HHS Public Access

Author manuscript

Dalton Trans. Author manuscript; available in PMC 2020 April 09.

Published in final edited form as:

Dalton Trans. 2019 April 09; 48(15): 5007–5021. doi:10.1039/c9dt00308h.

Mn^{IV}-oxo Complex of a Bis(benzimidazolyl)-containing N5 Ligand Reveals Different Reactivity Trends for Mn^{IV}-oxo than Fe^{IV}-oxo Species

Melissa C. Denler[a,±], **Allyssa A. Massie**[a,±], **Reena Singh**[b], **Eleanor Stewart-Jones**[a], **Arup Sinha**[b], **Victor W. Day**[a], **Ebbe Nordlander**[b], and **Timothy A. Jackson**[*,a]

[a]Department of Chemistry and Center for Environmentally Beneficial Catalysis, The University of Kansas, 1567 Irving Hill Road, Lawrence, KS 66045, USA.

[b]Department of Chemistry, Lund University, Chemical Physics, Box 124, SE-221 00 Lund, Sweden.

Abstract

Using the pentadentate ligand (*N*-bis(1-methyl-2-benzimidazolyl)methyl-*N*-(bis-2-pyridylmethyl)amine, 2pyN2B), presenting two pyridyl and two (*N*-methyl)benzimidazolyl donor moieties in addition to a central tertiary amine, new Mn^{II} and Mn^{IV}-oxo complexes were generated and characterized. The $[Mn^{IV}(O)(2pyN2B)]^{2+}$ complex showed spectroscopic signatures (*i.e.*, electronic absorption band maxima and intensities, EPR signals, and Mn K-edge X-ray absorption edge and near-edge data) similar to those observed for other Mn^{IV}-oxo complexes with neutral, pentadentate N_5 supporting ligands. The near-IR electronic absorption band maximum of $[Mn^{IV}(O)(2pyN2B)]^{2+}$, as well as DFT-computed metric parameters, are consistent with the equatorial (*N*-methyl)benzimidazolyl ligands being stronger donors to the Mn^{IV} center than the pyridyl and quinolinyl ligands found in analogous Mn^{IV}-oxo complexes. The hydrogen- and oxygen-atom transfer reactivities of $[Mn^{IV}(O)(2pyN2B)]^{2+}$ were assessed through reactions with hydrocarbons and thioanisole, respectively. When compared with related Mn^{IV}-oxo adducts, $[Mn^{IV}(O)(2pyN2B)]^{2+}$ showed muted reactivity in hydrogen-atom transfer reactions with hydrocarbons. This result stands in contrast to observations for the analogous Fe^{IV}-oxo complexes, where $[Fe^{IV}(O)(2pyN2B)]^{2+}$ was found to be one of the more reactive members of its class.

Graphical Abstract

[*]To whom correspondence should be addressed: Timothy A. Jackson, Phone: (785) 864-3968, taj@ku.edu.
± These authors made contributions of equal merit.

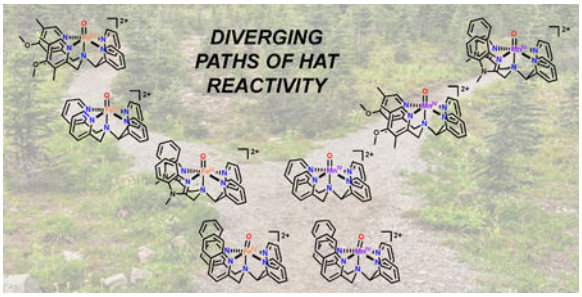

Introduction

The use of earth-abundant metal catalysts to effect hydrocarbon oxidation has grown significantly in recent years. These efforts have led to new non-porphyrinoid Fe- and Mn-based catalysts for C–H bond functionalization.[1–5] Catalytic mechanisms for these systems typically feature substrate oxidation by hydrogen- or oxygen-atom transfer steps (HAT and OAT, respectively) initiated by high-valent metal-oxo species. Our understanding of these catalysts is aided by structure-reactivity relationships obtained through investigations of stoichiometric reactions of isolable metal-oxo species. For example, we recently reported that Mn^{IV}-oxo adducts supported by derivatives of the pentadentate N4py ligand display HAT and OAT reaction rates that are dependent on the equatorial ligand field strength (Figure 1).[6] The N4py derivatives previously considered were ^{DMM}N4py and 2pyN2Q (Figure 1), which respectively feature electron-rich di-3,5-methyl-4-methoxy-pyridyl groups and bulky quinolinyl groups that serve to increase (for ^{DMM}N4py) and decrease (for 2pyN2Q) the equatorial ligand field of the Mn center relative to the parent N4py ligand. A DFT structure of $[Mn^{IV}(O)(2pyN2Q)]^{2+}$ showed that the steric bulk of the quinolinyl groups also crowds the oxo coordination position, causing a N_{axial}–Mn=O angle of 170°, with the oxo ligand tilted away from the quinolinyl moieties (Figure 1). DFT structures for the corresponding $[Mn^{IV}(O)(N4py)]^{2+}$ and $[Mn^{IV}(O)(^{DMM}N4py)]^{2+}$ complexes showed N_{axial} –Mn=O angles of almost exactly 180°. The $[Mn^{IV}(O)(2pyN2Q)]^{2+}$ complex showed reaction rates with a variety of hydrocarbons that were ca. 100-fold faster than those of $[Mn^{IV}(O)(^{DMM}N4py)]^{2+}$ (Figure 1). A larger, 4000-fold rate enhancement was observed for thioanisole oxidation by $[Mn^{IV}(O)(2pyN2Q)]^{2+}$ compared to $[Mn^{IV}(O)(^{DMM}N4py)]^{2+}$.

More recently, Que and co-workers reported similar rate enhancements for the analogous Fe^{IV}-oxo series,[7] where $[Fe^{IV}(O)(2pyN2Q)]^{2+}$ reacts with hydrocarbons ca. 20–50-fold faster than $[Fe^{IV}(O)(^{DMM}N4py)]^{2+}$.[8] An X-ray crystal structure of $[Fe^{IV}(O)(2pyN2Q)]^{2+}$ showed a N_{axial}–Fe=O angle near 170°, consistent with our DFT predictions from the $[Mn^{IV}(O)(2pyN2Q)]^{2+}$ complex. This angle contrasts with the analogous N_{axial}–Fe=O angle found in the X-ray structure of $[Fe^{IV}(O)(2pyN2B)]^{2+}$, for which the value is 177° (2pyN2B is an N4py derivative with two pyridyl and two *N*-(methyl)benzimidazolyl functions (Figure 1)).[7] The Fe^{IV}-oxo rate enhancements were also correlated with the Fe^{IV} ligand-field strength, as a linear relationship was observed between the HAT energy barrier (from $\log(k_2)$) and the average Fe–$N_{equatorial}$ distance from the X-ray crystal structures of the Fe^{IV}-oxo complexes. The $[Fe^{IV}(O)(2pyN2B)]^{2+}$ complex showed HAT and OAT reactions

rates approximately 1–2 orders of magnitude faster than the parent $[Fe^{IV}(O)(N4py)]^{2+}$ but 2–10 times slower than that of $[Fe^{IV}(O)(2pyN2Q)]^{2+}$.[7, 9]

To determine the influence of *N*-(methyl)benzimidazolyl ligation on a Mn^{IV}-oxo unit, we describe here the Mn^{IV}-oxo adduct supported by the 2pyN2B ligand, ($[Mn^{IV}(O)(2pyN2B)]^{2+}$; see Figure 1). To assess the influence of the 2pyN2B ligand on Mn^{IV}-oxo electronic structure and reactivity, we performed thorough spectroscopic investigations of $[Mn^{IV}(O)(2pyN2B)]^{2+}$, including characterization by electronic absorption, EPR, and Mn K-edge X-ray absorption near-edge spectroscopies. The reactivity of $[Mn^{IV}(O)(2pyN2B)]^{2+}$ was explored using thioanisole and 9,10-dihydroanthracene (DHA) as model substrates for OAT and HAT reactions, respectively. A comparison of the rates of $[Mn^{IV}(O)(2pyN2B)]^{2+}$ with those of related Mn^{IV}-oxo and Fe^{IV}-oxo complexes reveals a distinctly different relationship between ligand structure and reactivity for the Mn^{IV}-oxo adducts as compared to their Fe^{IV}-oxo analogues.

Experimental Methods

Materials and Instrumentation.

All chemicals and solvents were purchased from commercial vendors and were ACS reagent-grade quality or better. 9–10-dihydroanthracene (DHA) and xanthene were recrystallized from ethanol.[10] All other chemicals were used as received, with the exception of MeCN and diethylether, which were sparged with argon and dried as described previously.[11] $Mn^{II}(OTf)_2$•$2CH_3CN$, used for preparation of metal complexes, was synthesized according to a previously reported procedure.[12] For O_2-free reactions, solvents were dried following published procedures and degased by freeze-pump-thaw methods.[10] Iodosobenzene (PhIO) was prepared from iodosobenzene diacetate following a published procedure.[13]

Electronic absorption spectra for formation and kinetic reactions were obtained on a Varian Cary 50 Bio or an Agilent 8453 spectrophotometer. Both spectrophotometers were interfaced with Unisoku cryostats (USP-203-A), capable of maintaining temperatures of 25 °C for all reactions. Electrospray-ionization mass spectrometry experiments were performed using an LCT Primers Micromass electrospray time-of-flight instrument. NMR data were collected on a Bruker AVIIIHD 400 MHz NMR instrument. EPR data were collected between 5 and 10 K on a 9 GHz Bruker EMXPlus spectrometer with an Oxford ESR900 continuous-flow liquid helium cryostat controlled by an Oxford ITC503 temperature system. Perpendicular-mode data were collected in a dual-mode Bruker ER4116DM cavity. Recording conditions were 9.637 GHz microwave frequency, 2.0 mW microwave power, 6 G modulation amplitude, 100 kHz modulation frequency, and 141 ms time constant.

Synthesis and Characterization.

2pyN2B was synthesized by a previously published method.[9] The $[Mn^{II}(OH_2)(2pyN2B)](OTf)_2$ complex ($C_{31}H_{29}F_6MnN_7O_7S_2$) was prepared by reacting equimolar amounts of the 2pyN2B free ligand and $Mn^{II}(OTf)_2$•$2CH_3CN$ in CH_3CN under an argon atmosphere and

stirring the resultant solution for 30 minutes to an hour. Solid $[Mn^{II}(OH_2)(2pyN2B)](OTf)_2$ was obtained by slow diffusion of diethyl ether into the $[Mn^{II}(OH_2)(2pyN2B)](OTf)_2$ acetonitrile solution under argon. Repeated recrystallizations yielded the $[Mn^{II}(OH_2)(2pyN2B)](OTf)_2$ salt in 52% yield. ESI-MS data for $[Mn^{II}(OH_2)(2pyN2B)](OTf)_2$ dissolved in MeCN shows a single peak at 563.13 corresponding to $[Mn^{II}(2pyN2B)(Cl)]^+$, in which the triflate ion was replaced by a chloride in the mass spectrometer (Figure S2). The effective magnetic moment (μ_{eff}) of $[Mn^{II}(OH_2)(2pyN2B)](OTf)_2$ was found to be 5.91 μ_b, which is in good agreement with the expected μ_{eff} of 5.92 μ_b for high-spin Mn^{II} centers. The perpendicular-mode EPR spectrum of a 1 mM solution of $[Mn^{II}(OH_2)(2pyN2B)](OTf)_2$ was collected at 10 K (Figure S2). The intermediate $[Mn^{IV}(O)(2pyN2B)]^{2+}$ ($C_{29}H_{27}MnN_7O$) was prepared *in situ* by reacting 1.7 mg (0.002 mmol) $[Mn^{II}(OH_2)(2pyN2B)](OTf)_2$ with 4.4 mg (0.02 mmol) PhIO in 2.0 mL 2,2,2-trifluoroethanol (TFE). An ESI-MS sample of $[Mn^{IV}(O)(2pyN2B)]^{2+}$ was prepared by diluting 20 μL of the solution in pre-cooled MeCN (−40 ºC). ESI-MS data for isotopically-labeled $[Mn^{IV}(O)(2pyN2B)]^{2+}$ was obtained by incubating $[Mn^{IV}(O)(2pyN2B)]^{2+}$ with 15 μL $H_2{}^{18}O$ for 5 minutes to allow for water exchange. Because the stability of $[Mn^{IV}(O)(2pyN2B)]^{2+}$ is greatly reduced in MeCN, the dominant peaks in the mass spectra come from Mn^{II} decay products (Figure S3).

X-ray Crystallography of $[Mn^{II}(OH_2)(2pyN2B)](OTf)_2$.

Crystals suitable for characterization by X-ray diffraction were obtained by vapor diffusion of diethyl ether into an acetonitrile solution of $[Mn^{II}(OH_2)(2pyN2B)](OTf)_2$. A full hemisphere of diffracted intensities (740 15-second frames with a scan width of 1.00°) was measured for a single-domain specimen using graphite-monochromated Mo Kα radiation (λ = 0.71073 Å) on a Bruker SMART APEX CCD Single Crystal Diffraction System.[14] The integrated data[15] were corrected empirically for variable absorption effects using equivalent reflections. The Bruker software package SHELXTL was used to solve the structure using "direct methods" techniques. All stages of the weighted full-matrix least-squares refinement were conducted using F_o^2 data with the SHELXTL XL v2014 software package.[16] The final structural model incorporated anisotropic thermal parameters for all nonhydrogen atoms and isotropic thermal parameters for all hydrogen atoms. All hydrogen atoms for the metal complex were located with a difference Fourier and initially included in the structural model as independent isotropic atoms whose parameters were allowed to vary in least-squares refinement cycles. The methyl group was eventually included as an idealized sp^3-hydridized rigid rotor that was allowed to rotate freely about its C-C bond in refinement cycles. Hydrogen atoms for the ether molecule of crystallization were placed at idealized riding model positions with C-H bond lengths of 0.97 – 0.98 Å and isotropic thermal parameters that were 1.2 (nonmethyl) or 1.5 (methyl) times the equivalent isotropic thermal parameter of the carbon atom to which they were covalently bonded. The methyl groups in the ether molecule were placed with idealized "staggered" orientations and the rigid rotor methyl group in the metal complex utilized C-H bond lengths of 0.97 Å. Crystal data and structure refinement details are given in Table S1.

Preparation of XAS Sample.

A 15 mM sample of $[Mn^{II}(OH_2)(2pyN2B)](OTf)_2$ was prepared by dissolving 9.3 mg (0.012 mmol) $[Mn^{II}(OH_2)(2pyN2B)](OTf)_2$ in 0.8 mL of ethanol, transferring the solution to an

XAS sample holder, and flash freezing the solution in liquid nitrogen. A 10 mM XAS sample of $[Mn^{IV}(O)(2pyN2B)]^{2+}$ was prepared by dissolving 13.3 mg (0.016 mmol) $[Mn^{II}(OH_2)(2pyN2B)](OTf)_2$ in 1.6 mL of a TFE solution containing 35.2 mg PhIO (0.16 mmol). The reaction mixture was placed into a 0.2 cm cuvette, where the formation of $[Mn^{IV}(O)(2pyN2B)]^{2+}$ was monitored by electronic absorption spectroscopy. At maximum formation, two XAS samples were prepared and flash frozen in liquid nitrogen.

XAS Data Collection.

Mn K-edge XAS data for $[Mn^{IV}(O)(2pyN2B)]^{2+}$ were collected at beamline 9–3 at the Stanford Synchrotron Radiation Light Source (SSRL). XAS spectra for $[Mn^{IV}(O)(2pyN2B)]^{2+}$ were obtained as fluorescence excitation spectra using a Canberra 100-element Ge array detector. Data for $[Mn^{II}(OH_2)(2pyN2B)](OTf)_2$ was collected at beamline 2–2 at SSRL using a Si(111) monochromator and a 13-element Ge array fluorescence detector. Mn K-edge X-ray absorption spectra were collected over an energy range of 6.3 to 7.4 keV (Si(220) monochromator). The frozen samples were maintained at 7 K during data collection by an Oxford liquid He cryostat. A reference spectrum of a manganese foil was collected for each scan and an internal calibration was performed by setting the zero crossing of the second derivative of the K-edge energy of the reference spectra to 6539.0 keV. The high flux at beamline 9–3 lead to photo-reduction for $[Mn^{IV}(O)(2pyN2B)]^{2+}$. When multiple scans were collected on a single spot of the frozen sample for $[Mn^{IV}(O)(2pyN2B)]^{2+}$, there was a noticeable shift of the edge to a lower energy. To reduce the effects of photoreduction, the beam was moved to different spots on the sample and only one scan was collected per spot. Three scans were collected for $[Mn^{IV}(O)(2pyN2B)]^{2+}$. Compared to conditions at beamline 9–3, beamline 2–2 has reduced X-ray flux. These conditions required the use of ethanol as the solvent rather than TFE, as the latter solvent leads to diminished X-ray fluorescence. The relatively low flux and smaller number of detectors at this beamline required the signal averaging of eighteen scans for $[Mn^{II}(OH_2)(2pyN2B)](OTf)_2$.

XAS Data Analysis.

XAS data analysis was performed using the Demeter software package.[17] Individual scans of raw data were analyzed and combined using Athena. Fits of the pre-edge area was performed using the FityK software.[18] Pre-edge intensity was normalized relative to the tail of the fluorescence signal.

EPR Sample Preparation.

A 1 mM sample of $[Mn^{II}(OH_2)(2pyN2B)](OTf)_2$ was prepared and flash frozen using liquid nitrogen in a 4 mm quartz EPR tube. A 10 mM sample of $[Mn^{IV}(O)(2pyN2B)]^{2+}$ was prepared by thawing the XAS sample at −20 °C and then immediately transferring 200 μL of this solution into a pre-cooled EPR tube and flash freezing the tube in liquid nitrogen.

Electronic Structure Computations.

All computations were performed using the *ORCA* 3.0.3 software package.[19] DFT geometry optimizations of $[Mn^{IV}(O)(2pyN2B)]^{2+}$ and $[Mn^{IV}(O)(N4py)]^{2+}$ employed the TPSS functional,[20] TZVP (Mn, O, and N) and SVP (C, F, and H) basis sets,[21–23] and the COSMO

solvation model (for TFE).[24] Tight optimization and SCF criteria were invoked using the TightOpt and TightSCF keywords. The RI approximation, with TZVP/J and SVP/J auxiliary basis sets, was used for geometry optimizations. This level of theory replicates that employed for previously reported geometries of $[Mn^{IV}(O)(2pyN2Q)]^{2+}$ and $[Mn^{IV}(O)(^{DMM}N4py)]^{2+}$,[6] allowing for a balanced structural comparison of these complexes. Structures were converged to the $S = 3/2$ spin states. Cartesian coordinates for $[Mn^{IV}(O)(2pyN2B)]^{2+}$ and $[Mn^{IV}(O)(N4py)]^{2+}$ are included in Tables S3 and S4.

HAT and OAT Reactivity Studies.

In a typical reaction, when 1.0 mM of $[Mn^{IV}(O)(2pyN2B)]^{2+}$ was fully formed, an aliquot of a solution containing substrate (thioanisole in TFE and DHA or xanthene in CH_2Cl_2) was added to the cuvette for a final solution volume of 2.1 mL. The decay of the 940 nm feature of $[Mn^{IV}(O)(2pyN2B)]^{2+}$ was monitored, and the resulting time trace was fit to a pseudo-first order model. The observed rate constants were plotted against the substrate concentration to obtain a second-order rate constant. For DHA, 10 – 40 equivalents of substrate were added to determine the second-order rate constant for HAT reactivity. The reaction of $[Mn^{IV}(O)(2pyN2B)]^{2+}$ with deuterated $[D_4]$-DHA was used to determine a primary kinetic isotope effect. For xanthene, 20–50 equivalents of substrate were added to determine the second-order rate constant for HAT reactivity. 10 to 60 equivalents of thioanisole were used to determine the second-order rate constant for the OAT reaction.

Product Analysis Experiments.

Analysis of the product of the reaction between $[Mn^{IV}(O)(2pyN2B)]^{2+}$ and DHA was performed by removing the solvent under vacuum and then re-dissolving the isolated residue in cyclohexane. The product anthracene was observed and quantified using the published extinction coefficient for anthracene in cyclohexane.[25] Analysis of the product of the reaction of $[Mn^{IV}(O)(2pyN2B)]^{2+}$ and thioanisole was performed by ^{1}H-NMR experiments following previously described methods.[6] The only modification was the use of toluene as internal standard, which was added directly to the ^{1}H-NMR sample before analysis.

Cyclic Voltammetry Experiments.

A glassy carbon working electrode, a platinum auxiliary electrode, and a Ag/AgCl quasi-reference electrode were used with an external ferrocene/ferrocenium potential as an external reference. Cyclic voltammograms were recorded on an Epsilon potentiostat. These experiments used 16.5 mg (0.02 mmol) $[Mn^{II}(OH_2)(2pyN2B)](OTf)_2$, with 22.0 mg PhIO (0.1 mmol) in TFE with 0.1 M Bu_4NPF_6 electrolyte at 298 K. Fewer equivalents of PhIO were used in electrochemical experiments due to limited solubility of PhIO in TFE.

Results and Discussion

X-ray Diffraction Structure of $[Mn^{II}(OH_2)(2pyN2B)](OTf)_2$.

The crystal structure of $[Mn^{II}(OH_2)(2pyN2B)](OTf)_2$ shows a mononuclear Mn^{II} center in a distorted octahedral environment with an axial water ligand and the 2pyN2B ligand bound in its expected pentadentate mode (Figure 2). The axial Mn−OH_2 distance of 2.087(3) Å is comparable to that observed for $[Mn^{II}(OH_2)(2pyN2Q)](OTf)_2$ (2.091(2) Å).[6] However, the

water ligand in $[Mn^{II}(OH_2)(2pyN2B)](OTf)_2$ is not as distorted from the idealized octahedral position as in $[Mn^{II}(OH_2)(2pyN2Q)](OTf)_2$ (N_{axial}–Mn–OH_2 angles of 177.9° and 163.8°, respectively). This difference in bond angles reflects the greater steric influence of the quinolinyl moieties in 2pyN2Q on the axial coordination position. In support, the closest contacts for the benzimidazolyl carbon atoms and the oxygen atom of the water ligand of $[Mn^{II}(OH_2)(2pyN2B)]^{2+}$ are 3.807 Å. These separations lead to corresponding CH···OH_2 interaction distances of 3.093 Å. In contrast, the previously reported XRD structure of $[Mn^{II}(OH_2)(2pyN2Q)](OTf)_2$ shows $C_{quinolinyl}$···OH_2 separations of 3.453 and 3.515 Å, which leads to much shorter CH···OH_2 interaction distances of 2.529 and 2.616 Å. The greater steric influence of the 2pyN2Q ligand as compared to 2pyN2B was also observed in the recently reported XRD structures for the Fe^{IV}-oxo complexes (*vide supra*).[7] As discussed by Que and coworkers, the steric influence exerted by the quinolinyl substituents leads to long metal-$N_{quinoline}$ distances and, consequently, weak quinolinyl donation to the metal.[2, 7]

The two Mn–$N_{benzimidazolyl}$ distances in $[Mn^{II}(OH_2)(2pyN2B)](OTf)_2$ are 2.193(2) Å, which are ca. 0.06 – 0.08 Å shorter than the corresponding Mn–$N_{pyridyl}$ distances of $[Mn^{II}(OTf)(N4py)]^+$, but similar to the Mn–$N_{3,5\text{-dimethyl-4-methoxypyridyl}}$ bond lengths of $[Mn^{II}(OTf)(^{DMM}N4py)]^+$ (Table 1).[6, 26] These short Mn–$N_{benzimidazolyl}$ distances are accordant with the greater basicity of benzimidazole than pyridine.[27] The Mn–$N_{pyridyl}$ distances of $[Mn^{II}(OH_2)(2pyN2B)](OTf)_2$ (2.298(2) Å) are comparable to those observed for the other Mn^{II} complexes (Table 1). Overall, the average Mn–$N_{equatorial}$ distance for $[Mn^{II}(OH_2)(2pyN2B)](OTf)_2$ is slightly less than that of $[Mn^{II}(OTf)(^{DMM}N4py)]^{2+}$ (2.246 and 2.251 Å, respectively), making the 2pyN2B ligand the *strongest* equatorial donor of this series. The largest Mn-ligand bond deviation for $[Mn^{II}(OH_2)(2pyN2B)](OTf)_2$ is in the Mn –N_{amine} bond distance (2.375(3) Å), which is nearly 0.09 Å longer than the corresponding distances for the other Mn^{II} structures (Table 1). The Fe^{II}–N_{amine} distance in $[Fe^{II}(2pyN2B)(NCMe)](ClO_4)_2$ showed a similar elongation of 0.067 Å relative to $[Fe^{II}(N4py)(NCMe)](ClO_4)_2$.[9] This variation in bond length was attributed to different angular requirements of the five-membered benzimidazolyl and six-membered pyridyl rings.[9] The same rationale can be applied to account for the elongated Mn–N_{amine} bond of $[Mn^{II}(OH_2)(2pyN2B)](OTf)_2$. When this elongated Mn–N_{amine} distance is considered, the average Mn–N distances of $[Mn^{II}(OH_2)(2pyN2B)](OTf)_2$ (Mn–N_{total} in Table 1) are just slightly less than those of $[Mn^{II}(OTf)(N4py)]^+$ and $[Mn^{II}(OH_2)(2pyN2Q)]^{2+}$, and longer than that of $[Mn^{II}(OTf)(^{DMM}N4py)]^+$ (Table 1). Collectively, these metric data show that 2pyN2B provides an equatorial ligand field comparable in strength to that of ^{DMM}N4py and stronger than that of N4py and 2pyN2Q but with markedly attenuated axial donation.

The trend in Mn–$N_{equatorial}$ bond length observed for the manganese(II) complexes with the 2pyN2B, N4py, and ^{DMM}N4py ligands is more dramatic than that observed for the corresponding iron(II) complexes. Specifically, $[Fe^{II}(MeCN)(2pyN2B)](ClO_4)_2$, $[Fe^{II}(MeCN)(N4py)](ClO_4)_2$, and $[Fe^{II}(MeCN)(^{DMM}N4py)](OTf)_2$ showed average Fe –$N_{equatorial}$ distances within the narrow range of 1.971 Å to 1.978 Å. This 0.007 Å length span is much smaller than the 0.038 Å variation seen for the corresponding Mn^{II} complexes (Table 1). The Fe^{II} complexes are all low spin ($S = 0$) at the temperatures employed for the X-ray crystallography experiments, and it is therefore expected that the Fe–$N_{equatorial}$

distances should be less sensitive to perturbations in the equatorial ligand field than the high-spin ($S = 5/2$) Mn^{II} complexes, in which the metal $3d_{x^2-y^2}$ MO, which is metal-$N_{equatorial}$ σ-antibonding, will be populated. [8–9, 28]

Formation and characterization of $[Mn^{IV}(O)(2pyN2B)]^{2+}$.

The addition of PhIO to a TFE solution of $[Mn^{II}(OH_2)(2pyN2B)](OTf)_2$ at 25 °C led to the formation of new electronic absorption bands at 940, 460, and 410 nm (Figure 3). These bands reached maximum intensity when 10 equivalents of PhIO were used. The energy and intensity of the near-IR absorption band at 940 nm (ε = 250 $M^{-1}cm^{-1}$, assuming 100% formation) is quite similar to that observed for Mn^{IV}-oxo complexes of the N4py, ^{DMM}N4py, and 2pyN2Q ligands (λ_{max} = 920 – 1180 nm; ε = 179 – 290 $M^{-1}cm^{-1}$; Table 2).[6, 26] On the basis of this similarity, and strongly supported by additional data described below, we assign the chromophore formed by the reaction of $[Mn^{II}(OH_2)(2pyN2B)](OTf)_2$ with PhIO to $[Mn^{IV}(O)(2pyN2B)]^{2+}$. In previous investigations of $[Mn^{IV}(O)(N4py)]^{2+}$ and its derivatives, the near-IR absorption bands of these complexes were attributed to the $^4B_1 \rightarrow {}^4E$ transition, which corresponds to a one-electron excitation from the quasi-degenerate Mn^{IV} $3d_{xz}$ and $3d_{yz}$ MOs to the unoccupied $3d_{x^2-y^2}$ MO.[6, 29] These MOs are Mn=O π-antibonding and Mn −$N_{equatorial}$ σ-antibonding, respectively. Previous DFT computations for $[Mn^{IV}(O)(N4py)]^{2+}$ and its derivatives showed that variations in the energy of this electronic transition arise predominantly from perturbations in Mn−$N_{equatorial}$ bonding.[6, 29] As shown in Table 2, the near-IR absorption maxima of $[Mn^{IV}(O)(2pyN2B)]^{2+}$ (940 nm; 10 640 cm^{-1}) lies between those of $[Mn^{IV}(O)(^{DMM}N4py)]^{2+}$ (920 nm; 10 870 cm^{-1}) and $[Mn^{IV}(O)(N4py)]^{2+}$ (950 nm; 10 530 cm^{-1}). This position is consistent with the benzimidazolyl moieties being better σ-donors than an unmodified pyridine, as also manifested in the Mn^{II}–N_X distances of the corresponding Mn^{II} complexes (Table 1).

Even when using 10 equivalents PhIO, the rate of formation of $[Mn^{IV}(O)(2pyN2B)]^{2+}$ was relatively slow, taking about 20 minutes to reach completion. ESI-MS data for $[Mn^{IV}(O)(2pyN2B)]^{2+}$ show an ion peak at *m/z* of 272.08 (Figure S3), which agrees with that predicted for the Mn^{IV}-oxo adduct (*m/z* of 272.08). When $[Mn^{IV}(O)(2pyN2B)]^{2+}$ is incubated with $H_2{}^{18}O$, the ESI-MS shows a new peak at 273.08, which indicates water exchange to give the Mn^{IV}-^{18}O adduct (Figure S3). At 25 °C in TFE, a 1.0 mM solution of $[Mn^{IV}(O)(2pyN2B)]^{2+}$ showed a half-life of ~2.7 hours (Figure S4), which falls between those of $[Mn^{IV}(O)(2pyN2Q)]^{2+}$ and $[Mn^{IV}(O)(^{DMM}N4py)]^{2+}$ (half-lives of 0.2 and 6 hours, respectively). The thermal decay product of $[Mn^{IV}(O)(2pyN2B)]^{2+}$ is EPR silent and shows prominent ESI-MS peaks at 662.15 and 726.18, which correspond to $[Mn^{III}(2pyN2B)(OCH_2CF_3)(Cl)]^+$ and $[Mn^{III}(2pyN2B)(OCH_2CF_3)_2]^+$, respectively (Figure S5).

The X-band, perpendicular-mode EPR spectrum for $[Mn^{IV}(O)(2pyN2B)]^{2+}$ is characterized by a broad, positive feature centered at g_{eff} = 5.7, a weak derivative signal near g_{eff} = 2.9, and a multiline signal around g_{eff} = 2 (Figure 3, bottom left). The signal at g_{eff} = 5.7 shows a six-line hyperfine splitting with a = 7.0 mT. The multiline signal at g_{eff} = 2 likely derives from a multi-nuclear Mn species, which we assign as a $Mn^{III}Mn^{IV}$ dimer (Supplementary Information).[30] Although the g_{eff}-values for $[Mn^{IV}(O)(2pyN2B)]^{2+}$ are in the range expected for mononuclear, S = 3/2 Mn^{IV} species,[31] the spectrum is perturbed compared to

those observed for the other N4py-based oxomanganese(IV) complexes (Figure S6 and Table 2).[6, 26] The down-field shift of the g_{eff} = 5.7 signal for $[Mn^{IV}(O)(2pyN2B)]^{2+}$, and the appearance of the weak signal at g_{eff} = 2.9, suggests that this oxomanganese(IV) complex has a larger rhombic component to its zero-field splitting tensor (*i.e.*, larger *E/D* parameter, where *D* and *E* are the axial and rhombic zero-field splitting parameters, respectively). The EPR spectrum of $[Mn^{IV}(O)(2pyN2B)]^{2+}$ is reminiscent of that observed for $[Mn^{IV}(O)(OH)(Me_2EBC)]^{+}$ (Me_2EBC = 4,11-dimethyl-1,4,8,11-tetraazabicyclo[6.6.2]hexadecane), which had two overlapping six-line hyperfine features at g_{eff} = 5.95 and 4.99, and a derivative signal at g_{eff} = 2.62.[31]

Cyclic voltammetry (CV) data for $[Mn^{IV}(O)(2pyN2B)]^{2+}$ show an irreversible one-electron reduction at −0.07 V vs. Cp_2Fe/Cp_2Fe^{+} (+0.47 V vs. SCE; see Figure S7), which is attributed to the $Mn^{III/IV}$ couple. This process is irreversible, even at scan rates up to 1000 mV s^{-1}. The observed peak potential is slightly less than that of $[Mn^{IV}(O)(^{DMM}N4py)]^{2+}$ (0.06 V vs. Cp_2Fe/Cp_2Fe^{+} or +0.61 V vs. SCE), and over 0.5 V less than $[Mn^{IV}(O)(2pyN2Q)]^{2+}$, which has the highest potential for this series (Table 2).[6] The low peak potential for $[Mn^{IV}(O)(2pyN2B)]^{2+}$ is consistent with the short $Mn-N_{benzimidazolyl}$ distances observed in the X-ray structure of $[Mn^{II}(OH_2)(2pyN2B)](OTf)_2$ (Figure 2), which suggest that the benzimidazolyl ligands are stronger donors than the pyridyl or quinolinyl ligands. Although peak potentials have not been reported for the analogous $[Fe^{IV}(O)(2pyN2B)]^{2+}$ complex, we can compare the shift observed between $[Mn^{IV}(O)(2pyN2B)]^{2+}$ and $[Mn^{IV}(O)(N4py)]^{2+}$ with that reported for their Fe^{II} analogues. In that case, the $[Fe^{II}(NCMe)(2pyN2B)]^{2+}$ complex had a potential 0.45 V less than that of $[Fe^{II}(NCMe)(N4py)]^{2+}$ (0.398 and 0.85 V versus Cp_2Fe/Cp_2Fe^{+}, respectively).[9] The 0.33 V lower potential of $[Mn^{IV}(O)(2pyN2B)]^{2+}$ than $[Mn^{IV}(O)(N4py)]^{2+}$ is comparable (Table 2).

Mn K-edge X-ray absorption data for $[Mn^{II}(OH_2)(2pyN2B)]^{+}$ and $[Mn^{IV}(O)(2pyN2B)]^{2+}$ show a 2.5 eV increase in edge energy for the latter complex (Figure 4), which is consistent with the higher Mn oxidation state. The edge energy of $[Mn^{IV}(O)(2pyN2B)]^{2+}$ (6549.6 eV) is also very similar to those observed for other Mn^{IV}-oxo complexes with neutral pentadentate ligands (6549.2 – 6550.8 eV).[6, 26] The observation that the edge energy of $[Mn^{IV}(O)(2pyN2B)]^{2+}$ is on the lower end of those observed for related Mn^{IV}-oxo adducts is congruent with the EPR data for this complex, which shows a weak multiline signal (Figure 3) due to the presence of some multinuclear species (potentially a $Mn^{III}Mn^{IV}$ dimer).

The XAS spectrum of $[Mn^{IV}(O)(2pyN2B)]^{2+}$ shows a prominent pre-edge feature centered at ca. 6541 eV (Figure 4) with an area of 14.6 units (Figure S8). This feature is readily attributed to a Mn^{IV} 1s-to-3d transition, which gains intensity through Mn^{IV} 3d-4p mixing induced by the short Mn=O distance. The previously described $[Mn^{IV}(O)(N4py)]^{2+}$, $[Mn^{IV}(O)(^{DMM}N4py)]^{2+}$, and $[Mn^{IV}(O)(2pyN2Q)]^{2+}$ complexes also showed pre-edge features near 6541 eV (Figure S9),[6, 26] with areas ranging from 17.0 – 19.6 units.

Electronic Structure Computations for $[Mn^{IV}(O)(2pyN2B)]^{2+}$.

DFT calculations were carried out to further understand the geometric and electronic structure of $[Mn^{IV}(O)(2pyN2B)]^{2+}$. The DFT-optimized structure of $[Mn^{IV}(O)(2pyN2B)]^{2+}$

has a Mn=O bond length of 1.671 Å, which is very similar to those predicted for the Mn^{IV}-oxo complexes of the ^{DMM}N4py, N4py, and 2pyN2Q ligands (1.673 – 1.678 Å; see Figure 5 and Table S2). While the Mn–$N_{equatorial}$ distances of $[Mn^{IV}(O)(2pyN2B)]^{2+}$ are the shortest of the series (2.011 Å; see Figure 5 and Table S2), they are only slightly shorter than the Mn –$N_{equatorial}$ distances of $[Mn^{IV}(O)(^{DMM}N4py)]^{2+}$ and $[Mn^{IV}(O)(N4py)]^{2+}$ (2.015 and 2.018 Å, respectively). These predictions are consistent with the similar near-IR λ_{max} values of these complexes (Table 2), which we had previously shown reflect the equatorial ligand-field strength.[6, 29] Further, the Mn–$N_{equatorial}$ distances of $[Mn^{IV}(O)(2pyNQ)]^{2+}$ are significantly elongated at 2.054 Å, consistent with the larger perturbation in the near-IR λ_{max} of this complex (Table 2). These variations in metal-nitrogen equatorial bond lengths are qualitatively similar to that observed in the crystal structures of the corresponding Fe^{IV}-oxo complexes.[7] In that case, the average Fe^{IV}–$N_{equatorial}$ bond length of $[Fe^{IV}(O)(2pyN2Q)]^{2+}$ was significantly elongated (2.046 Å), while those of $[Fe^{IV}(O)(2pyN2B)]^{2+}$ and $[Fe^{IV}(O)(N4py)]^{2+}$ were quite similar (1.971 and 1.956 Å, respectively). Nonetheless, for the Fe^{IV}-oxo complexes, N4py provides a stronger equatorial ligand field than 2pyN2B, whereas DFT computations for the corresponding Mn^{IV}-oxo complexes predicts 2pyN2B to be a stronger equatorial donor (Figure 5 and Table S2).

The Mn–N_{amine} bond in the DFT-optimized structure of $[Mn^{IV}(O)(2pyN2B)]^{2+}$ is elongated compared to the other Mn^{IV}-oxo complexes (Figure 5 and Table S2). This result is in agreement with the Mn^{II} XRD structures, where the Mn–N_{amine} bond of $[Mn^{II}(OH_2)(2pyN2B)](OTf)_2$ was also longer than that of the other Mn^{II} complexes. The DFT structure also demonstrates that the 2pyN2B ligand provides significantly less steric crowding of the oxo compared to the 2pyN2Q ligand. This is exemplified by the O–Mn–N_{amine} angle of 177.48°, which is less distorted than in $[Mn^{IV}(O)(2pyN2Q)]^{2+}$ (O–Mn–N_{amine} angle of 170.14°). For comparison, we note that $[Mn^{II}(OH_2)(2pyN2B)](OTf)_2$ also showed a less distorted O–Mn–N_{amine} angle of 177.9°, while the corresponding angle in $[Mn^{II}(OH_2)(2pyN2Q)](OTf)_2$ is 163.8°.

Hydrocarbon and Thioanisole Oxidation by $[Mn^{IV}(O)(2pyN2B)]^{2+}$.

To further compare $[Mn^{IV}(O)(2pyN2B)]^{2+}$ with other Mn^{IV}-oxo adducts, we investigated the reactivity of this complex with hydrocarbons and thioanisole. These reactions are expected to occur by different mechanisms (HAT and OAT, respectively), allowing us to understand the influence of the *N*-(methyl)benzimidazolyl functions in $[Mn^{IV}(O)(2pyN2B)]^{2+}$ on two separate reaction types. Our prior investigation of $[Mn^{IV}(O)(N4py)]^{2+}$, $[Mn^{IV}(O)(^{DMM}N4py)]^{2+}$, and $[Mn^{IV}(O)(2pyN2Q)]^{2+}$ revealed correlations between HAT and OAT reaction rates with both the near-IR absorption energy and the $Mn^{III/IV}$ reduction potentials of these complexes.[6] In each case, faster rates were associated with a more positive $Mn^{III/IV}$ reduction potential and a lower-energy near-IR absorption band. The basis for correlations with the near-IR absorption band are provided by DFT computations, which predict that HAT and OAT reactions for $[Mn^{IV}(O)(N4py)]^{2+}$ and related Mn^{IV}-oxo complexes involve crossing from the $^4B_1$ ground state to a ^4E excited state (arising from a Mn^{IV} $e(d_{xz}, d_{yz}) \rightarrow b_1(d_{x^2-y^2})$ one-electron excitation).[32–33] Our MCD investigations of $[Mn^{IV}(O)(N4py)]^{2+}$ assigned the near-IR absorption maxima of this complex as an excitation to the ^4E excited state.[29] Thus, according to this two-state reactivity model,

complexes with lower-energy near-IR absorption bands (lower ^{4}E excited-state energies) should have lower transition states for HAT and OAT reactions. Alternatively, the $Mn^{III/IV}$ reduction potential represents a portion of the driving force for the HAT and OAT process, with more positive potentials being associated with a larger driving force. The $[Mn^{IV}(O)(2pyN2B)]^{2+}$ complex provides an interesting test for these correlations, as this complex shows the lowest $Mn^{III/IV}$ $E_{p,c}$ values for this series, but has a near-IR absorption maximum between those of $[Mn^{IV}(O)(N4py)]^{2+}$ and $[Mn^{IV}(O)(^{DMM}N4py)]^{2+}$ (Table 2).

Treatment of 1.0 mM $[Mn^{IV}(O)(2pyN2B)]^{2+}$ in TFE with an excess of 9,10-dihydroanthracene (DHA) at 25 °C led to the decay of the Mn^{IV}-oxo electronic absorption signals by pseudo-first-order and isosbestic behavior (Figure 6, top). The pseudo-first order rate constants, obtained by fitting the disappearance of the 940 nm band of $[Mn^{IV}(O)(2pyN2B)]^{2+}$ over time (Figuer 6, top inset), showed a linear increase as a function of increasing DHA concentration (Figure 6, center). This analysis yielded a second-order rate constant (k_2) of 0.27(2) $M^{-1}s^{-1}$. To determine any solvent influence on this rate, we performed analogous kinetic investigations for the reaction of DHA with $[Mn^{IV}(O)(2pyN2B)]^{2+}$ in 1:1 (vol:vol) TFE:CH_2Cl_2, which yielded a smaller k_2 of 0.16(1) $M^{-1}s^{-1}$ (Figure S10). This slight influence of solvent on the rate is similar to that observed for $[Mn^{IV}(O)N4py]^{2+}$,[26] and reinforces other reports of modest enhancements for HAT reaction rates in TFE .[34] The rate of DHA oxidation by $[Mn^{IV}(O)(2pyN2B)]^{2+}$ in 1:1 TFE:CH_2Cl_2 is two-fold slower than that observed for $[Mn^{IV}(O)(^{DMM}N4py)]^{2+}$ (k_2 = 0.34(2) $M^{-1}s^{-1}$ in 1:1 TFE:CH_2Cl_2), which had shown the slowest rate of DHA oxidation for Mn^{IV}-oxo complexes of N4py and its derivatives (Table 2).[6, 26] To further compare the HAT reactivity of $[Mn^{IV}(O)(2pyN2B)]^{2+}$ with that of $[Mn^{IV}(O)(^{DMM}N4py)]^{2+}$, we determined the rate of reaction of $[Mn^{IV}(O)(2pyN2B)]^{2+}$ with xanthene, which has a weaker C–H bond than DHA (bond dissociation free energies of 73.3 kcal/mol vs 76.0 kcal/mol, respectively).[35] The oxidation of xanthene by $[Mn^{IV}(O)(2pyN2B)]^{2+}$ gave k_2 = 0.39(2) $M^{-1}s^{-1}$ in 1:1 TFE:CH_2Cl_2 (Figure S11). This rate is slightly slower than that observed for $[Mn^{IV}(O)(^{DMM}N4py)]^{2+}$ in 1:1 TFE:CH_2Cl_2 (k_2 of 0.62(6) $M^{-1}s^{-1}$), showing that $[Mn^{IV}(O)(2pyN2B)]^{2+}$ is the slower oxidant for two hydrocarbons.

To probe the mechanism of hydrocarbon oxidation by $[Mn^{IV}(O)(2pyN2B)]^{2+}$, analogous kinetic experiments were performed using deuterated [D_4]-DHA. The decay of the near-IR feature of $[Mn^{IV}(O)(2pyN2B)]^{2+}$ in the presence of [D_4]-DHA was significantly slower than that observed for DHA (Figure S12 and S13), and a comparison of k_2 values yielded an H/D kinetic isotope effect of 12.5. This value is similar to that observed for $[Mn^{IV}(O)(^{DMM}N4py)]^{2+}$ and $[Mn^{IV}(O)(N4py)]^{2+}$ (10.2 and 11.2, respectively)[6, 26] and is suggestive of a HAT mechanism. Oxidation of 1.0 equivalent of DHA by $[Mn^{IV}(O)(2pyN2B)]^{2+}$ produced 0.4 equivalents anthracene per equivalent Mn^{IV}-oxo complex, also similar to that reported for DHA oxidation by $[Mn^{IV}(O)(N4py)]^{2+}$ and $[Mn^{IV}(O)(^{DMM}N4py)]^{2+}$.[6, 26] Additionally, ESI-MS of the solution following the reaction showed two prominent peaks at 563.14 and 662.15, corresponding to $[Mn^{II}(2pyN2B)(Cl)]^+$ and $[Mn^{III}(2pyN2B)(OCH_2CF_3)(Cl)]^+$ respectively (Figure S14). Thus, DHA oxidation by $[Mn^{IV}(O)(2pyN2B)]^{2+}$ gives a mixture of Mn^{II} and Mn^{III} products.

We also probed the reactivity of $[Mn^{IV}(O)(2pyN2B)]^{2+}$ with thioanisole. Unlike the hydrocarbons considered previously, thioanisole should react with this Mn^{IV}-oxo complex by an OAT mechanism. The addition of 40 equivalents thioanisole to a 1.0 mM solution of $[Mn^{IV}(O)(2pyN2B)]^{2+}$ in TFE at 25 °C led to a rapid disappearance of the electronic absorption bands at 405 and 940 nm by a first-order process for up to 3 half-lives (Figure S16). This reaction was accompanied by a slight increase in absorption intensity at 610 nm, with isosbestic points at 540 and 720 nm. We observed an increase in the decay rate of $[Mn^{IV}(O)(2pyN2B)]^{2+}$ as a function of thioanisole concentration, giving a second-order rate constant (k_2) of 0.028(3) $M^{-1}s^{-1}$ in TFE (Table 3 and Figure 6, bottom). This rate is intermediate between those of $[Mn^{IV}(O)(^{DMM}N4py)]^{2+}$ and $[Mn^{IV}(O)(N4py)]^{2+}$ (k_2 of 0.0023(4) and 0.060(3) $M^{-1}s^{-1}$, respectively), and is 300-fold slower than that of $[Mn^{IV}(O)(2pyN2Q)]^{2+}$ (k_2 = 9.2(9) $M^{-1}s^{-1}$).[6, 26] ^{1}H NMR analysis performed after the reaction of $[Mn^{IV}(O)(2pyN2B)]^{2+}$ with 60 equivalents of thioanisole showed methylphenylsulfoxide in 50% yield relative to the starting Mn^{II} concentration.

Correlations for HAT and OAT Reactions of Mn^{IV}-oxo Species.

The present data for HAT and OAT reactions of $[Mn^{IV}(O)(2pyN2B)]^{2+}$ allow us to revisit our prior correlations of these reaction rates with the λ_{max} of the near-IR absorbance feature of the Mn^{IV}-oxo complexes and the $Mn^{III/IV}$ reduction potentials.[1, 6] Figure 7 shows the relationships between the barriers for DHA oxidation by the Mn^{IV}-oxo complexes (represented as $\log(k_2)$) vs. the $Mn^{III/IV}$ reduction potential and the near-IR transition energy. DHA oxidation by $[Mn^{IV}(O)(2pyN2B)]^{2+}$ occurs at a rate expected on the basis of the reduction potential of this complex (Figure 7, squares), thereby reinforcing this correlation. In contrast, $[Mn^{IV}(O)(2pyN2B)]^{2+}$ is an outlier for the previously observed correlation between the near-IR transition energy and the rate of DHA oxidation via hydrogen atom transfer. While the near-IR λ_{max} of $[Mn^{IV}(O)(2pyN2B)]^{2+}$ lies midway between those of $[Mn^{IV}(O)(N4py)]^{2+}$ and $[Mn^{IV}(O)(^{DMM}N4py)]^{2+}$ (Table 2 and Figure 7), $[Mn^{IV}(O)(2pyN2B)]^{2+}$ shows a rate of reaction with DHA that is slower than that of both these complexes. Thus, for HAT reactions of these Mn^{IV}-oxo complexes with DHA, the $Mn^{III/IV}$ reduction potential is a better indicator of reactivity than the ^{4}E excited-state energy (taken as the near-IR λ_{max} value).

A similar comparison of OAT reaction rates of Mn^{IV}-oxo complexes vs. $Mn^{III/IV}$ reduction potential and near-IR λ_{max} values is presented in Figure 8. For these OAT reactions, there is a close correlation between the OAT reaction barrier and the energy of the near-IR electronic absorption band (Figure 8, triangles). In particular, $[Mn^{IV}(O)(2pyN2B)]^{2+}$ shows a near-IR band quite similar in energy to that of $[Mn^{IV}(O)(N4py)]^{2+}$, which is in keeping with their similar rates of reaction with thioanisole (Figure 8). This correlation is consistent with DFT predictions that the ^{4}E excited state is involved in OAT reactions of Mn^{IV}-oxo complexes.[32] In contrast, $[Mn^{IV}(O)(2pyN2B)]^{2+}$ has a rate substantially faster than expected on the basis of its reduction potential (Figure 8, squares). Specifically, $[Mn^{IV}(O)(2pyN2B)]^{2+}$ has a lower potential than $[Mn^{IV}(O)(^{DMM}N4py)]^{2+}$ and $[Mn^{IV}(O)(N4py)]^{2+}$ (by 0.14 and 0.33 V, respectively), but reacts with thioanisole 10-fold faster than $[Mn^{IV}(O)(^{DMM}N4py)]^{2+}$ and only 2-fold slower than $[Mn^{IV}(O)(N4py)]^{2+}$ (Table 2). The lack of a correlation between the thioanisole oxidation rate and the $Mn^{III/IV}$ potentials of these Mn^{IV}-oxo complexes is not

unexpected, as thioanisole oxidation presumably occurs by an OAT mechanism, which is a two-electron process.

Comparison of Mn^{IV}-oxo and Fe^{IV}-oxo Reactivity at Parity of Ligand Coordination Sphere.

The present kinetic investigations of $[Mn^{IV}(O)(2pyN2B)]^{2+}$ also allow us to compare variations in HAT and OAT rates of these Mn^{IV}-oxo adducts with those of Fe^{IV}-oxo complexes supported by the same series of ligands. For the Mn^{IV}-oxo complexes, $[Mn^{IV}(O)(2pyN2Q)]^{2+}$ displays the fastest rate of reaction with DHA, with $[Mn^{IV}(O)(^{DMM}N4py)]^{2+}$ and $[Mn^{IV}(O)(2pyN2B)]^{2+}$ showing roughly similar rates that are the slowest for the series (Figure 9). These rates give an overall ligand ordering of 2pyN2Q > N4py > ^{DMM}N4py ≈ 2pyN2B for HAT reactions of the Mn^{IV}-oxo adducts. For the Fe^{IV}-oxo analogues, we can compare ligand effects using reaction rates for ethylbenzene oxidation, which show an ordering of 2pyN2Q > 2pyN2B > N4py ≈ ^{DMM}N4py (Figure 9). In this case, $[Fe^{IV}(O)(2pyN2Q)]^{2+}$ shows a rate of reaction with ethylbenzene that is only 2-fold faster than that of $[Fe^{IV}(O)(2pyN2B)]^{2+}$.[7] Additionally, $[Fe^{IV}(O)(2pyN2B)]^{2+}$ reacts with ethylbenzene 12-fold faster than $[Fe^{IV}(O)(N4py)]^{2+}$, with even more dramatic rate enhancements observed for other substrates.[9] The HAT reactivity of $[Fe^{IV}(O)(^{DMM}N4py)]^{2+}$ and $[Fe^{IV}(O)(N4py)]^{2+}$ are quite similar, with the latter complex showing a faster rate of reaction with ethylbenzene (Figure 9) but a slower rate with cumene (Figure S20).[8, 39]

There is also data available to compare the OAT rates of Mn^{IV}-oxo and Fe^{IV}-oxo complexes supported by the N4py, 2pyN2B, and 2pyN2Q ligands. As was the case for the HAT reactions, both $[Mn^{IV}(O)(2pyN2Q)]^{2+}$ and $[Fe^{IV}(O)(2pyN2Q)]^{2+}$ show greatly enhanced reactivity towards thioanisole (Figure S20). For the Fe^{IV}-oxo series, $[Fe^{IV}(O)(2pyN2B)]^{2+}$ showed the next highest reactivity with $[Fe^{IV}(O)(N4py)]^{2+}$ having the slowest rate.[9] In contrast, $[Mn^{IV}(O)(2pyN2B)]^{2+}$ displayed a thioanisole oxidation rate slightly less than that of $[Mn^{IV}(O)(N4py)]^{2+}$ (Table 3). Collectively, the rate data for both HAT and OAT reactions clearly demonstrates that identical ligand perturbations tune the reactivity of Fe^{IV}-oxo and Mn^{IV}-oxo complexes quite differently (Figure 9).

The observation that the oxometal(IV) complexes with 2pyN2Q ligation provide the fastest rates could be related to several unique features of these complexes. First, as shown in the DFT structure of $[Mn^{IV}(O)(2pyN2Q)]^{2+}$ and the X-ray crystal structure of $[Fe^{IV}(O)(2pyN2Q)]^{2+}$, the steric bulk of the quinolinyl moieties in these complexes crowds the oxo binding site, leading to a distortion in the N_{axial}–M=O bond angle from the 180° expected for an idealized six-coordinate complex.[6–7] For comparison, the $[Fe^{IV}(O)(2pyN2B)]^{2+}$ and $[Mn^{IV}(O)(2pyN2B)]^{2+}$ complexes show evidence of more modest steric interactions between the *N*(methyl)benzimidazolyl groups and the oxo ligand (Figure 5). Respective DFT and X-ray crystallographic results for these complexes show N_{axial}–M=O bond angles of 177°. The influence, if any, of this relatively small bond angle distortion on the reactivity of these complexes is unclear at present.

The second influence of the quinolinyl functions is to provide weaker metal-nitrogen bonds than the pyridyl and *N*(methyl)benzimidazolyl donors in the other complexes. For $[Mn^{IV}(O)(2pyN2Q)]^{2+}$, this effect is apparent in both the extremely low energy of the near-IR absorption band maxima (reflecting the stabilization of Mn^{IV} $3d_{x^2-y^2}$ MO that is σ-

antibonding with respective to the equatorial ligands) and the high $Mn^{III/IV}$ reduction potential (Table 2). For $[Fe^{IV}(O)(2pyN2Q)]^{2+}$, $Fe–N_{quinolinyl}$ bond elongations relative to comparable Fe–N distances are readily apparent in the X-ray crystal structure.[7] As has been discussed above, this is suggested to be a consequence of the steric interactions between the quinolinyl moieties and the $Fe^{IV}(O)$ entity, leading to a weaker effective field being exerted by these substituents. For the Fe^{IV}-oxo series, the relationship between these bond elongations and HAT and OAT reaction rates was displayed through a correlation between the average Fe^{IV}–N distances of these complexes and the barriers (expressed as $\log(k_2)$) for cyclohexane and thioanisole oxidation.[7] A similar correlation, using experimental Mn–N distances is not possible for the Mn^{IV}-oxo complexes, as experimental structural data are lacking for these complexes. The only common set of experimental metric parameters for the corresponding Mn systems comes from the X-ray crystal structures of the Mn^{II} complexes. Plots of the average Mn^{II}–N distance from these structures vs. $\log(k_2)$ for DHA and thioanisole oxidation show reasonable correlations, albeit with a fair amount of scatter (Figure 10, top-left panel). Far less scatter, especially for the DHA reactions, is observed when the average $Mn^{II}–N_{equatorial}$ distance is plotted versus the $\log(k_2)$ values (Figure 10, top-right panel). Analogous correlations developed using DFT-calculated Mn^{IV}–N distances show a fair degree of scatter (Figure 10, bottom panels). It should be noted that the variation in average Mn^{IV}–N distances is quite small (from 2.033 Å for $[Mn^{IV}(O)(^{DMM}N4py)]^{2+}$ to 2.065 Å for $[Mn^{IV}(O)(2pyN2Q)]^{2+}$. For comparison, the average crystallographic Fe–N distances of $[Fe^{IV}(O)(N4py)]^{2+}$ and $[Fe^{IV}(O)(2pyN2Q)]^{2+}$ vary by 0.08 Å (1.972 and 2.053 Å, respectively).

Comba, Sastri, and co-workers have also observed a different pattern of reactivity for Mn^{IV}-oxo and Fe^{IV}-oxo complexes at parity of ligand sphere.[40–41] Their work employed pentadentate bispidine ligands (termed L_1 and L_2), whose different architectures place different amine functions *trans* to the oxo binding site.[41] Kinetic examination of thioanisole and 2,4-di-*tert*-butylphenol oxidation by $[Mn^{IV}(O)(L_1)]^{2+}$ and $[Mn^{IV}(O)(L_2)]^{2+}$ provided faster rates for the former complex. In contrast, the $[Fe^{IV}(O)(L_2)]^{2+}$ species is a more rapid oxidant than $[Fe^{IV}(O)(L_1)]^{2+}$.[40, 42–43] DFT analysis of cyclohexane oxidation by this set of metal-oxo species revealed that the Fe^{IV}-oxo adducts react with this hydrocarbon through the so-called σ-pathway (linear Fe–O–H angle in the transition state), while the Mn^{IV}-oxo adducts utilize the π-pathway (bent Mn–O–H angle in the transition state). It was further proposed that, because of the distinctly different transition state structures, electronic factors dominant in the Fe^{IV}-oxo species, whereas steric factors are dominant for the Mn^{IV}-oxo species.[41] While intriguing, it is unclear whether this model can explain the different reactivity patterns of the Mn^{IV}-oxo and Fe^{IV}-oxo complexes considered in this present work. For example, Figure 7 shows a reasonable correlation between the HAT reaction barrier and the $Mn^{III/IV}$ reduction potential, suggesting that this electronic parameter, and not some steric factor, can account for the reactivity ordering of these complexes. Nonetheless, the basis for the disparate reactivity patterns of these Mn^{IV}-oxo and Fe^{IV}-oxo species is unclear at present. Further experimental and computational work is needed to fully explain these observations.

Conclusions.

In this work, we have described new Mn^{II} and Mn^{IV}-oxo complexes supported by the 2pyN2B ligand that features a mixture of amine, pyridyl, and *N*(methyl)benzimidazolyl donors. The $[Mn^{IV}(O)(2pyN2B)]^{2+}$ complex features a Mn^{IV}-oxo unit whose spectroscopic signatures resemble those of $[Mn^{IV}(O)(N4py)]^{2+}$ and its analogues $[Mn^{IV}(O)(^{DMM}N4py)]^{2+}$ and $[Mn^{IV}(O)(2pyN2Q)]^{2+}$. The near-IR electronic absorption band maxima of $[Mn^{IV}(O)(2pyN2B)]^{2+}$, which corresponds to a Mn^{IV} $e(d_{xz}, d_{yz}) \rightarrow b_1(d_x{}^2{}_{-y}{}^2)$ one-electron excitation, lies between those of $[Mn^{IV}(O)(^{DMM}N4py)]^{2+}$ and $[Mn^{IV}(O)(N4py)]^{2+}$, illustrating the higher donor strength of the *N*(methyl)benzimidazolyl functions compared to unsubstituted pyridyl groups. With regard to chemical reactivity, the rate of reaction of $[Mn^{IV}(O)(2pyN2B)]^{2+}$ with hydrocarbons was the slowest of the Mn^{IV}-oxo complexes supported by N4py and its derivatives. The slow rate was in keeping with the lower reduction potential of this complex. In contrast, $[Mn^{IV}(O)(2pyN2B)]^{2+}$ reacted with thioanisole with a rate close to that of $[Mn^{IV}(O)(N4py)]^{2+}$ and roughly ten-fold faster than that of $[Mn^{IV}(O)(^{DMM}N4py)]^{2+}$. These trends in reactivity for this set of Mn^{IV}-oxo complexes contrast with that observed for the Fe^{IV}-oxo analogues. In those systems, the $[Fe^{IV}(O)(2pyN2B)]^{2+}$ complex is more reactive than $[Fe^{IV}(O)(^{DMM}N4py)]^{2+}$ and $[Fe^{IV}(O)(N4py)]^{2+}$. Although the basis for these disparate ligand influences are unclear at present, these observations illustrate that design principles developed for tuning the reactivity of Fe^{IV}-oxo complexes cannot be applied *carte blanche* to Mn^{IV}-oxo analogues, and *vice versa*.

Supplementary Material

Refer to Web version on PubMed Central for supplementary material.

Acknowledegements.

This work was supported by the U.S. D.O.E. (DE-SC0016359). A.S. thanks the Carl Trygger Foundation for a postdoctoral fellowship. M.C.D. was supported by the NIH Graduate Traineeship T32 GM08545. The U.S. N.S.F. is acknowledged for funds used to support the purchase of EPR and X-ray instrumentation (CHE-0946883 and CHE-0923449). Use of beamline 9–3 at the Stanford Synchrotron Radiation Lightsource, SLAC National Accelerator Laboratory, is supported by the U.S. Department of Energy, Office of Science, Office of Basic Energy Sciences under Contract No. DE-AC02–76SF00515. The SSRL Structural Molecular Biology Program is supported by the DOE Office of Biological and Environmental Research, and by the National Institutes of Health, National Institute of General Medical Sciences (including P41GM103393). The contents of this publication are solely the responsibility of the authors and do not necessarily represent the official views of NIGMS or NIH. Use of Beamline 2–2 at SSRL was partially supported by the National Synchrotron Light Source II, Brookhaven National Laboratory, under U.S. Department of Energy Contract No. DE-SC0012704. XAS experiments were supported by the Case Western Reserve University Center for Synchrotron Biosciences NIH grant, P30-EB-009998, from the National Institute of Biomedical Imaging and Bioengineering (NIBIB). Support for the NMR instrumentation was provided by NIH Shared Instrumentation Grant # S10OD016360. We thank Prof. Matt Haukka at the University of Jyväskylä in Finland for structural data collection on CCDC entry 1891620.

References

1. Rice DB; Massie AA; Jackson TA, Manganese–Oxygen Intermediates in O–O Bond Activation and Hydrogen-Atom Transfer Reactions. Acc. Chem. Res. 2017, 50 (11), 2706–2717. [PubMed: 29064667]
2. Puri M; Que L, Toward the Synthesis of More Reactive S = 2 Non-Heme Oxoiron(IV) Complexes. Acc. Chem. Res. 2015, 48 (8), 2443–2452. [PubMed: 26176555]

3. Nam W; Lee Y-M; Fukuzumi S, Hydrogen Atom Transfer Reactions of Mononuclear Nonheme Metal–Oxygen Intermediates. Acc. Chem. Res. 2018, 51 (9), 2014–2022. [PubMed: 30179459]
4. Oloo WN; Que L, Bioinspired Nonheme Iron Catalysts for C–H and C═C Bond Oxidation: Insights into the Nature of the Metal-Based Oxidants. Acc. Chem. Res. 2015, 48 (9), 2612–2621. [PubMed: 26280131]
5. Milan M; Salamone M; Costas M; Bietti M, The Quest for Selectivity in Hydrogen Atom Transfer Based Aliphatic C–H Bond Oxygenation. Acc. Chem. Res. 2018, 51 (9), 1984–1995. [PubMed: 30080039]
6. Massie AA; Denler MC; Cardoso LT; Walker AN; Hossain MK; Day VW; Nordlander E; Jackson TA, Equatorial Ligand Perturbations Influence the Reactivity of Manganese(IV)-Oxo Complexes. Angew. Chem., Int. Ed. Engl. 2017, 56 (15), 4178–4182. [PubMed: 28300349]
7. Rasheed W; Draksharapu A; Banerjee S; Young VG; Fan R; Guo Y; Ozerov M; Nehrkorn J; Krzystek J; Telser J; Que L, Crystallographic Evidence for a Sterically Induced Ferryl Tilt in a Non-Heme Oxoiron(IV) Complex that Makes it a Better Oxidant. Angew. Chem., Int. Ed. Engl. 2018, 57 (30), 9387–9391. [PubMed: 29882390]
8. Rana S; Dey A; Maiti D, Mechanistic elucidation of C-H oxidation by electron rich non-heme iron(iv)-oxo at room temperature. Chem. Commun. 2015, 51 (77), 14469–14472.
9. Mitra M; Nimir H; Demeshko S; Bhat SS; Malinkin SO; Haukka M; Lloret-Fillol J; Lisensky GC; Meyer F; Shteinman AA; Browne WR; Hrovat DA; Richmond MG; Costas M; Nordlander E, Nonheme Fe(IVP) Oxo Complexes of Two New Pentadentate Ligands and Their Hydrogen-Atom and Oxygen-Atom Transfer Reactions. Inorg. Chem. 2015, 54 (15), 7152–7164. [PubMed: 26198840]
10. Armarego WLF; Perrin DD, Purification of Laboratory Chemicals. Butterworth-Heinemann: Oxford, U.K., 1997.
11. Wijeratne GB; Corzine B; Day VW; Jackson TA, Saturation Kinetics in Phenolic O–H Bond Oxidation by a Mononuclear Mn(III)–OH Complex Derived from Dioxygen. Inorg. Chem. 2014, 53 (14), 7622–7634. [PubMed: 25010596]
12. Seo MS; Kim JY; Annaraj J; Kim Y; Lee Y-M; Kim S-J; Kim J; Nam W, [Mn(tmc)(O2)]+: A Side-On Peroxide Manganese(III) Complex Bearing a Non-heme Ligand. Angew. Chem., Int. Ed. Engl. 2007, 46, 377–380. [PubMed: 17131439]
13. Saltzman H; Sharefkin JG, Iodosobenzene. Org. Synth. 1963, 43, 60.
14. Data Collection: SMART Software in APEX2 v2014.11–0 Suite. Bruker-AXS. 5465 E. Cheryl Parkway, Madison, WI 53711–5373 USA, 1998.
15. Data Reduction: SAINT Software in APEX2 v2014.11–0 Suite. Bruker-AXS, 5465 E. Cheryl Parkway, Madison, WI 53711–5373 USA.
16. Refinement: SHELXTL Software in APEX2 v2014.11–0 Suite. Bruker-AXS, 5465 E. Cheryl Parkway, Madison, WI 53711–5373 USA.
17. Ravel B; Newville M, ATHENA, ARTEMIS, HEPHAESTUS: data analysis for X-ray absorption spectroscopy using IFEFFIT. J. Synchrotron Rad. 2005, 12 (4), 537–541.
18. Wojdyr M, Fityk: a general-purpose peak fitting program. J. Appl. Cryst. 2010, 43 (5 Part 1), 1126–1128.
19. Neese F, The ORCA program system. WIREs Comput Mol Sci. 2012, 2 (1), 73–78.
20. Tao J; Perdew JP; Staroverov VN; Scuseria GE, Climbing the Density Functional Ladder: Nonempirical Meta\char21{}Generalized Gradient Approximation Designed for Molecules and Solids. Phys. Rev. Lett. 2003, 91 (14), 146401.
21. Schäfer A; Horn H; Ahlrichs R, Fully optimized contracted Gaussian basis sets for atoms Li to Kr. J. Chem. Phys. 1992, 97 (4), 2571–2577.
22. Schäfer A; Huber C; Ahlrichs R, Fully Optimized Contracted Gaussian Basis Sets of Triple Zeta Valence Quality for Atoms Li to Kr. J. Chem. Phys. 1994, 100, 5829–5835.
23. Weigend F; Ahlrichs R, Balanced basis sets of split valence, triple zeta valence and quadruple zeta valence quality for H to Rn: Design and assessment of accuracy. Phys. Chem. Chem. Phys. 2005, 7 (18), 3297–3305. [PubMed: 16240044]

24. Marenich AV; Cramer CJ; Truhlar DG, Universal Solvation Model Based on Solute Electron Density and on a Continuum Model of the Solvent Defined by the Bulk Dielectric Constant and Atomic Surface Tensions. J. Phys. Chem. B 2009, 113 (18), 6378–6396. [PubMed: 19366259]
25. Prahl S Anthracene. https://omlc.org/spectra/PhotochemCAD/html/022.html.
26. Leto DF; Ingram R; Day VW; Jackson TA, Spectroscopic properties and reactivity of a mononuclear oxomanganese(iv) complex. Chem. Commun. 2013, 49 (47), 5378–5380.
27. Lõkov M; Tshepelevitsh S; Heering A; Plieger PG; Vianello R; Leito I, On the Basicity of Conjugated Nitrogen Heterocycles in Different Media. Eur. J. Org. Chem. 2017, 2017 (30), 4475–4489.
28. Lubben M; Meetsma A; Wilkinson EC; Feringa B; Que L Jr., Nonheme Iron Centers in Oxygen Activation: Characterization of an Iron(III) Hydroperoxide Intermediate. Angew. Chem., Int. Ed. Engl. 1995, 34 (13–14), 1512–1514.
29. Leto DF; Massie AA; Rice DB; Jackson TA, Spectroscopic and Computational Investigations of a Mononuclear Manganese(IV)-Oxo Complex Reveal Electronic Structure Contributions to Reactivity. J. Am. Chem. Soc. 2016, 138 (47), 15413–15424. [PubMed: 27802057]
30. Lee Y; Jackson TA, Ligand Influence on Structural Properties and Reactivity of Bis(μ-oxo)dimanganese(III,IV) Species and Comparison of Reactivity with Terminal MnIV-oxo Complexes. ChemistrySelect 2018, 3 (47), 13507–13516.
31. Leto DF; Massie AA; Colmer HE; Jackson TA, X-Band Electron Paramagnetic Resonance Comparison of Mononuclear MnIV-oxo and MnIV-hydroxo Complexes and Quantum Chemical Investigation of MnIV Zero-Field Splitting. Inorg. Chem. 2016, 55 (7), 3272–3282. [PubMed: 27002928]
32. Chen J; Cho K-B; Lee Y-M; Kwon YH; Nam W, Mononuclear nonheme iron(iv)–oxo and manganese(iv)–oxo complexes in oxidation reactions: experimental results prove theoretical prediction. Chem. Commun. 2015, 51 (66), 13094–13097.
33. Cho K-B; Shaik S; Nam W, Theoretical Investigations into C–H Bond Activation Reaction by Nonheme MnIVO Complexes: Multistate Reactivity with No Oxygen Rebound. J. Phys. Chem. Lett. 2012, 3 (19), 2851–2856.
34. Massie AA; Sinha A; Parham JD; Nordlander E; Jackson TA, Relationship between Hydrogen-Atom Transfer Driving Force and Reaction Rates for an Oxomanganese(IV) Adduct. Inorg. Chem. 2018, 57 (14), 8253–8263. [PubMed: 29974738]
35. Warren JJ; Tronic TA; Mayer JM, Thermochemistry of Proton-Coupled Electron Transfer Reagents and its Implications. Chem. Rev. 2010, 110 (12), 6961–7001. [PubMed: 20925411]
36. Sawant SC; Wu X; Cho J; Cho K-B; Kim SH; Seo MS; Lee Y-M; Kubo M; Ogura T; Shaik S; Nam W, Water as an Oxygen Source: Synthesis, Characterization, and Reactivity Studies of a Mononuclear Nonheme Manganese(IV) Oxo Complex. Angew. Chem., Int. Ed. Engl. 2010, 49 (44), 8190–8194. [PubMed: 20859971]
37. Parsell TH; Yang M-Y; Borovik AS, C–H Bond Cleavage with Reductants: Re-Investigating the Reactivity of Monomeric MnIII/IV–Oxo Complexes and the Role of Oxo Ligand Basicity. J. Am. Chem. Soc. 2009, 131 (8), 2762–2763. [PubMed: 19196005]
38. Wu X; Seo MS; Davis KM; Lee Y-M; Chen J; Cho K-B; Pushkar YN; Nam W, A Highly Reactive Mononuclear Non-Heme Manganese(IV)–Oxo Complex That Can Activate the Strong C–H Bonds of Alkanes. J. Am. Chem. Soc. 2011, 133 (50), 20088–20091. [PubMed: 22091637]
39. Kaizer J; Klinker EJ; Oh NY; Rohde J-U; Song WJ; Stubna A; Kim J; Münck E; Nam W; Que L Jr., Nonheme FeIVO Complexes That Can Oxidize the C–H Bonds of Cyclohexane at Room Temperature. J. Am. Chem. Soc 2004, 126 (2), 472–473. [PubMed: 14719937]
40. Comba P; Maurer M; Vadivelu P, Oxidation of Cyclohexane by High-Valent Iron Bispidine Complexes: Tetradentate versus Pentadentate Ligands. Inorg. Chem. 2009, 48 (21), 10389–10396. [PubMed: 19813738]
41. Barman P; Vardhaman AK; Martin B; Wörner SJ; Sastri CV; Comba P, Influence of Ligand Architecture on Oxidation Reactions by High-Valent Nonheme Manganese Oxo Complexes Using Water as a Source of Oxygen. Angew. Chem., Int. Ed. Engl. 2015, 54 (7), 2095–2099. [PubMed: 25557423]

42. Bukowski MR; Comba P; Lienke A; Limberg C; Lopez de Laorden C; Mas-Ballesté R; Merz M; Que L Jr., Catalytic Epoxidation and 1,2-Dihydroxylation of Olefins with Bispidine–Iron(II)/H2O2 Systems. Angew. Chem., Int. Ed. Engl. 2006, 45 (21), 3446–3449. [PubMed: 16637091]

43. Jaccob M; Comba P; Maurer M; Vadivelu P; Venuvanalingam P, A combined experimental and computational study on the sulfoxidation by high-valent iron bispidine complexes. Dalton Trans. 2011, 40 (42), 11276–11281. [PubMed: 21959496]

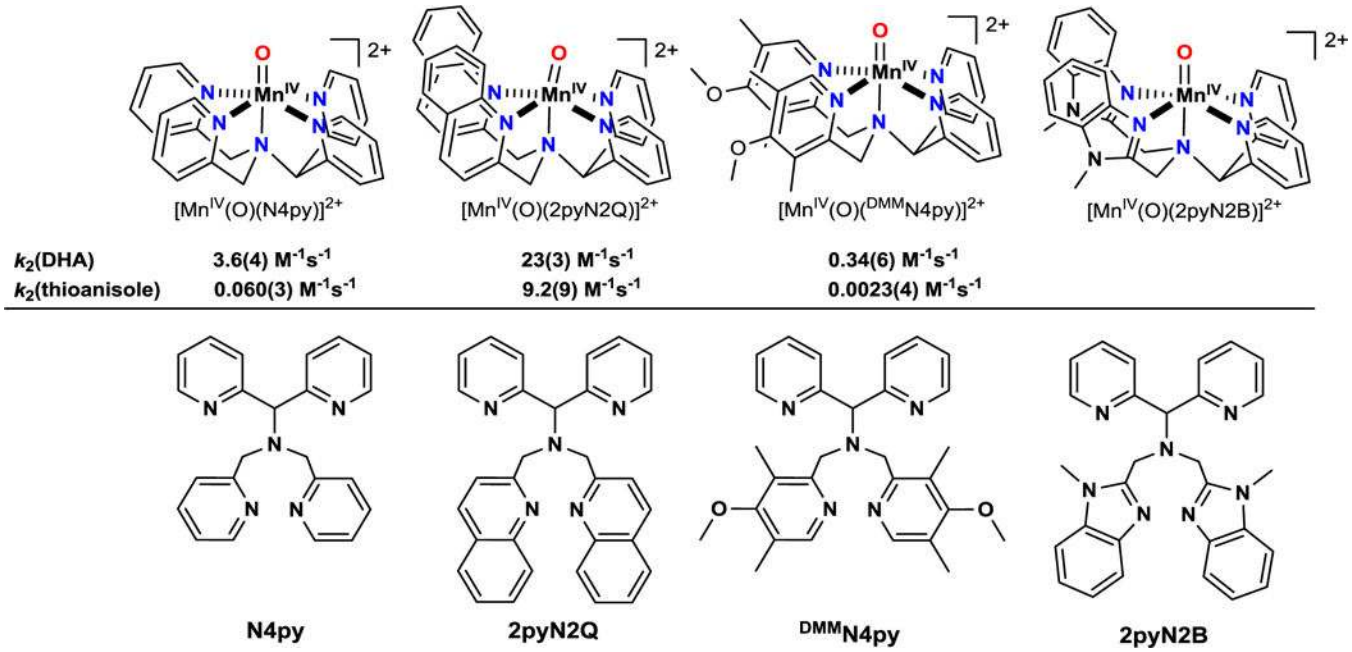

Figure 1.

Mn^{IV}-oxo complexes and ligands based on the N4py framework. Ligand abbreviations are as follows: N4py is *N*,*N*-bis(2-pyridylmethyl)-*N*-bis(2-pyridyl)methylamine; ^{DMM}N4py is *N*,*N*-bis(4-methoxy-3,5-dimethyl-2-pyridylmethyl)-*N*-bis(2-pyridyl)methylamine; 2pyN2Q is *N*,*N*-bis(2-pyridyl)-*N*,*N*-bis(2-quinolylmethyl)methanamine; and 2pyN2B is *N*,*N*-bis(1-methyl-2-benzimidazolyl)methyl-*N*-(bis-2-pyridylmethyl)-amine.

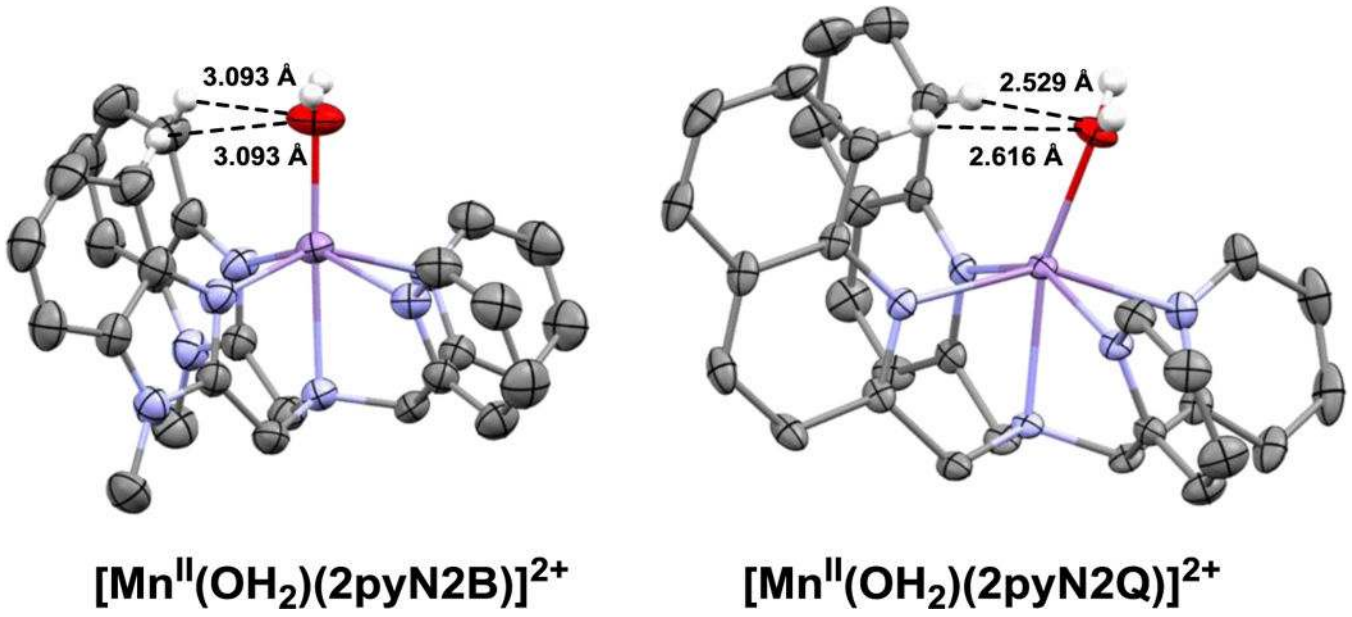

Figure 2.

Molecular structures of $[Mn^{II}(OH_2)(2pyN2B)]^{2+}$ and $[Mn^{II}(OH_2)(2pyN2Q)]^{2+}$ cations. Thermal ellipsoids are shown at 50% probability and most hydrogen atoms and triflate counter anions have been removed for clarity.

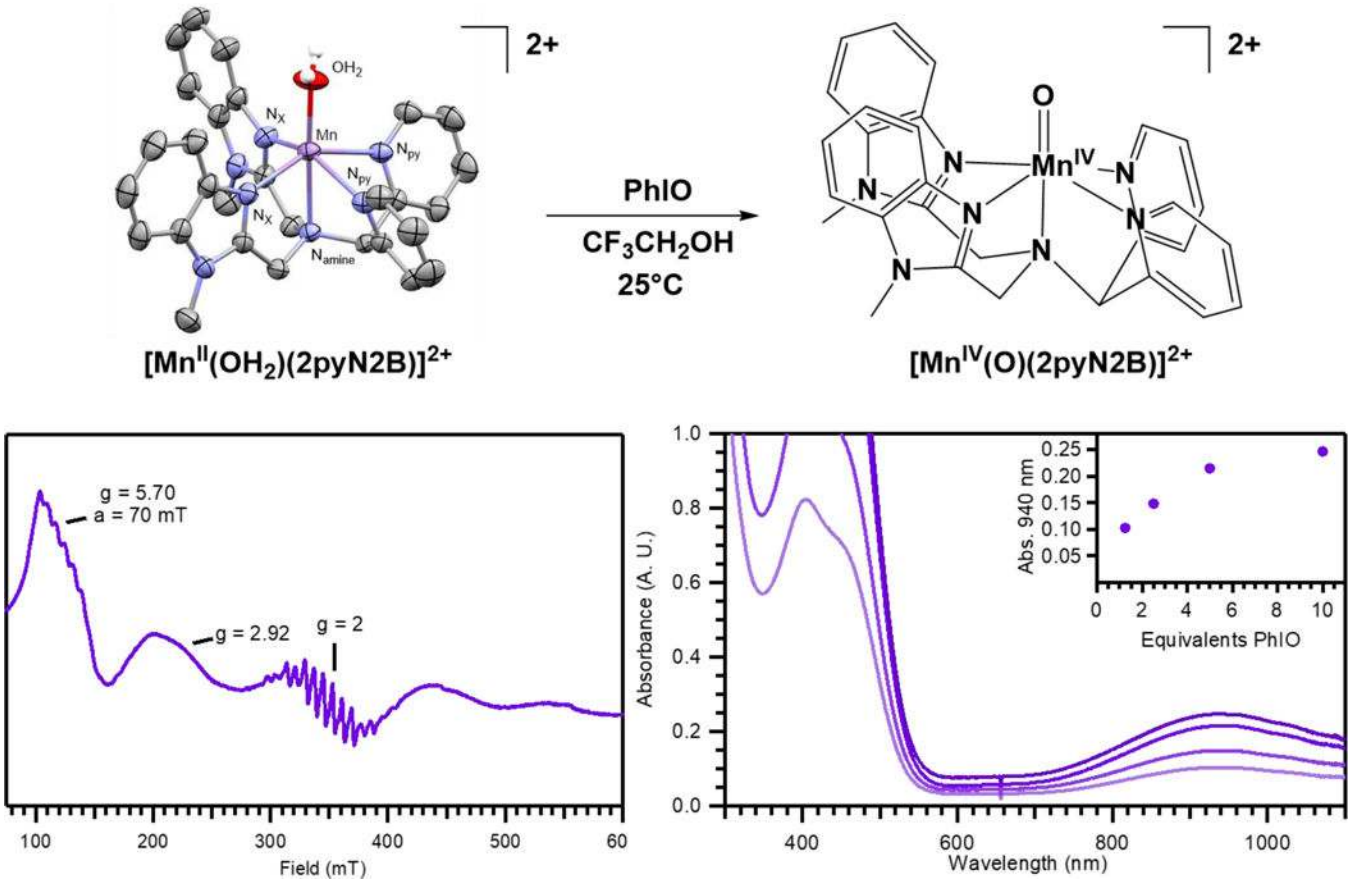

Figure 3.

Top: Formation of $[Mn^{IV}(O)(2pyN2B)]^{2+}$ from PhIO oxidation of $[Mn^{II}(OH_2)(2pyN2B)]^{2+}$. Bottom right: Electronic absorption spectra showing the final spectra of $[Mn^{IV}(O)(2pyN2B)]^{2+}$ following the addition of 1 to 10 equivalents PhIO to $[Mn^{II}(OH_2)(2pyN2B)](OTf)_2$ (1.0 mM in TFE at 25 °C). The inset shows the intensity of the near-IR absorption band as a function of equivalents PhIO. Bottom left: Perpendicular-mode X-band EPR spectra of $[Mn^{IV}(O)(2pyN2B)]^{2+}$ at 10 K.

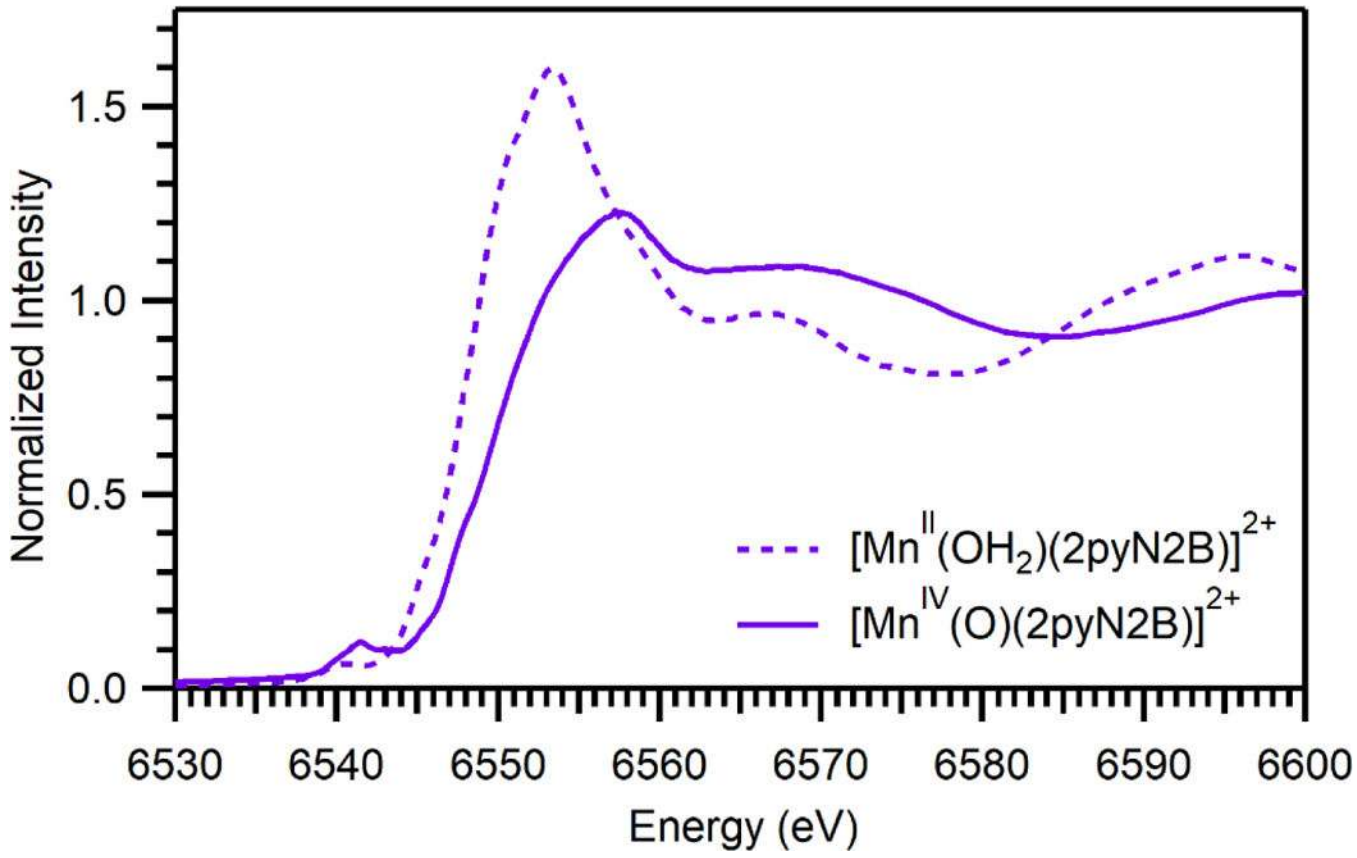

Figure 4.

Experimental XANES data for frozen samples of $[Mn^{II}(OH_2)(2pyN2B)](OTf)_2$ in ethanol (dashed traces) and $[Mn^{IV}(O)(2pyN2B)]^{2+}$ in TFE (solid traces).

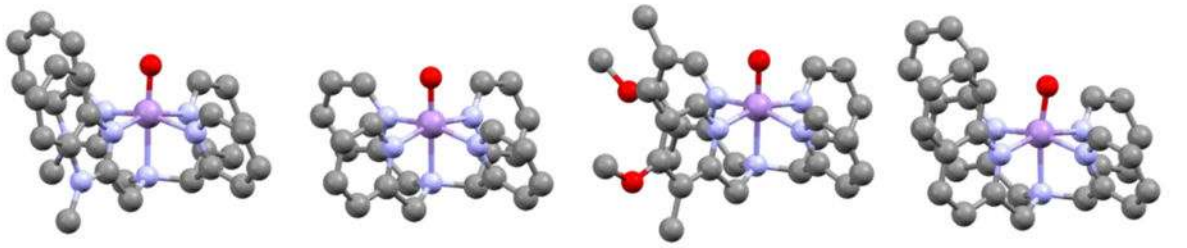

	$[Mn^{IV}(O)(2pyN2B)]^{2+}$	$[Mn^{IV}(O)(N4py)]^{2+}$	$[Mn^{IV}(O)(^{DMM}N4py)]^{2+}$	$[Mn^{IV}(O)(2pyN2Q)]^{2+}$
Mn–O	1.671 Å	1.673 Å	1.678 Å	1.678 Å
$Mn–N_{equatorial}$	2.011 Å	2.018 Å	2.015 Å	2.054 Å
$Mn–N_{amine}$	2.174 Å	2.118 Å	2.108 Å	2.109 Å
$Mn–N_{total}$	2.043 Å	2.038 Å	2.033 Å	2.065 Å
$O–Mn–N_{amine}$	177.48°	179.55°	179.76°	170.63°

Figure 5.

Selected Bond Lengths (Å), Bond Angles (°) from DFT Computations. $N_{equatorial}$ is the average of the four equatorial Mn–N bond lengths. N_{amine} refers to the amine nitrogen *trans* to the oxo ligand. N_{total} refers to the average of all Mn–N bond distances. Data for $[Mn^{IV}(O)(^{DMM}N4py)]^{2+}$, $[Mn^{IV}(O)(2pyN2Q)]^{2+}$ and $[Mn^{IV}(O)(N4py)]^{2+}$ have been published previously.[6, 26]

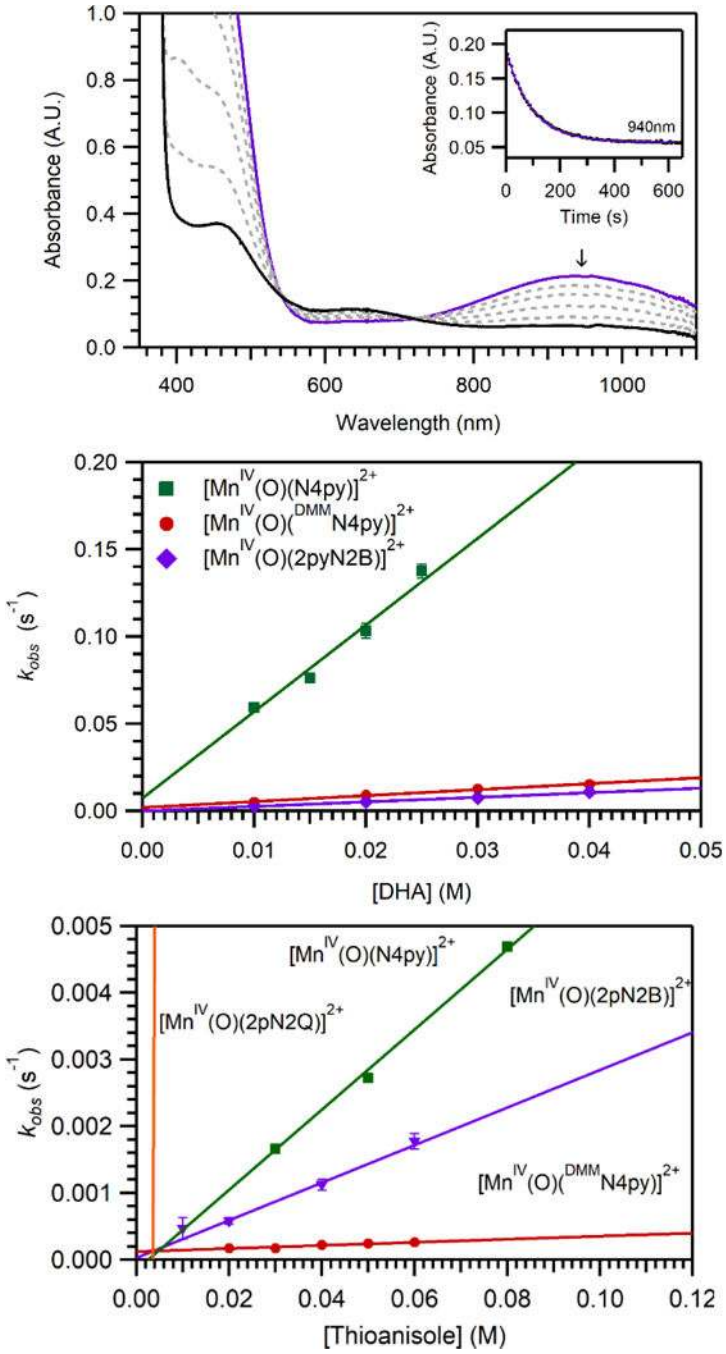

Figure 6.

Top: Electronic absorption spectra showing the decay of 1.0 mM $Mn^{IV}(O)(2pyN2B)]^{2+}$ (purple trace) upon addition of 40 equivalents DHA in TFE at 25 °C. The inset shows the decay of the feature at 940 nm. Center: Pseudo-first-order rate constants (k_{obs}) vs. DHA concentration for Mn^{IV}-oxo species. Bottom: Pseudo-first-order rate constants (k_{obs}) versus thioanisole concentration for oxomanganese(IV) species. For the center and bottom plots, the lines represent best fits to the data used to determine the second-order rate constants (k_2). Data for $[Mn^{IV}(O)(^{DMM}N4py)]^{2+}$, $[Mn^{IV}(O)(N4py)]^{2+}$, and $[Mn^{IV}(O)(2pyN2Q)]^{2+}$ are from

references [6] and [26]. As the rates of reaction for $[Mn^{IV}(O)(2pyN2Q)]^{2+}$ are substantially faster than those of the other complexes, the data points are off scale (see Figures S16 and S19 for plots with an expanded scale).

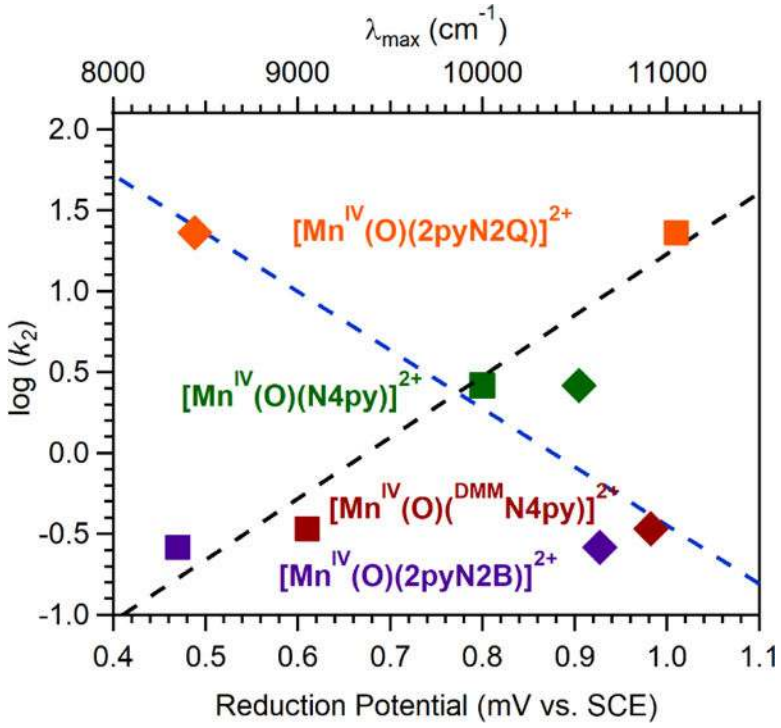

Figure 7.

Experimental log(k_2) values for DHA oxidation (HAT) by Mn^{IV}-oxo complexes versus $Mn^{III/IV}$ reduction potentials (squares, black line, bottom abscissa) and near-IR electronic absorption band maxima (diamonds, blue line, top abscissa). The fitted lines show the correlation between these parameters.

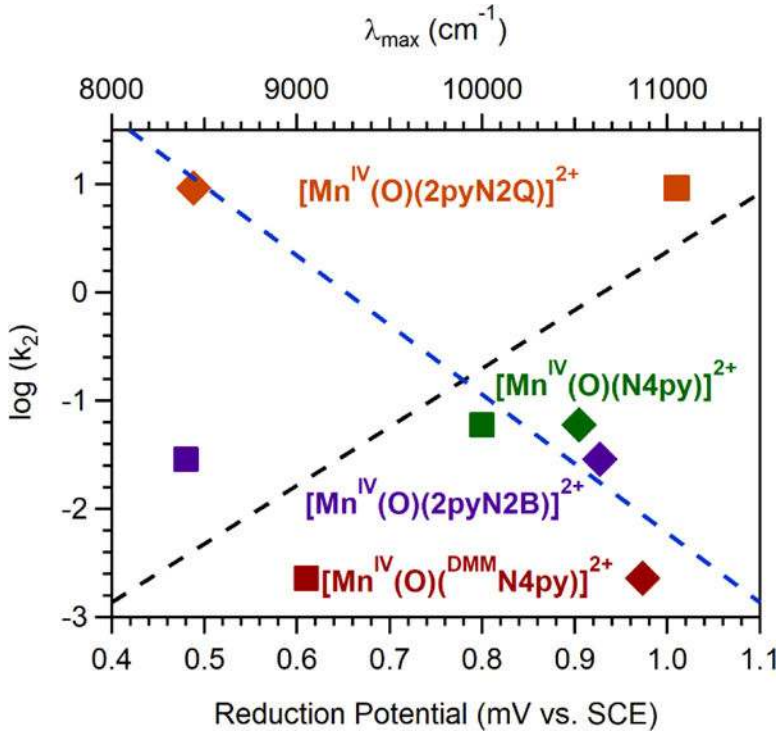

Figure 8.

Experimental log(k_2) values for thioanisole oxidation (OAT) by Mn^{IV}-oxo complexes versus $Mn^{III/IV}$ reduction potentials (squares, black line, bottom abscissa) and near-IR electronic absorption band maxima (diamonds, blue line, top abscissa). The fitted lines show the correlation between these parameters.

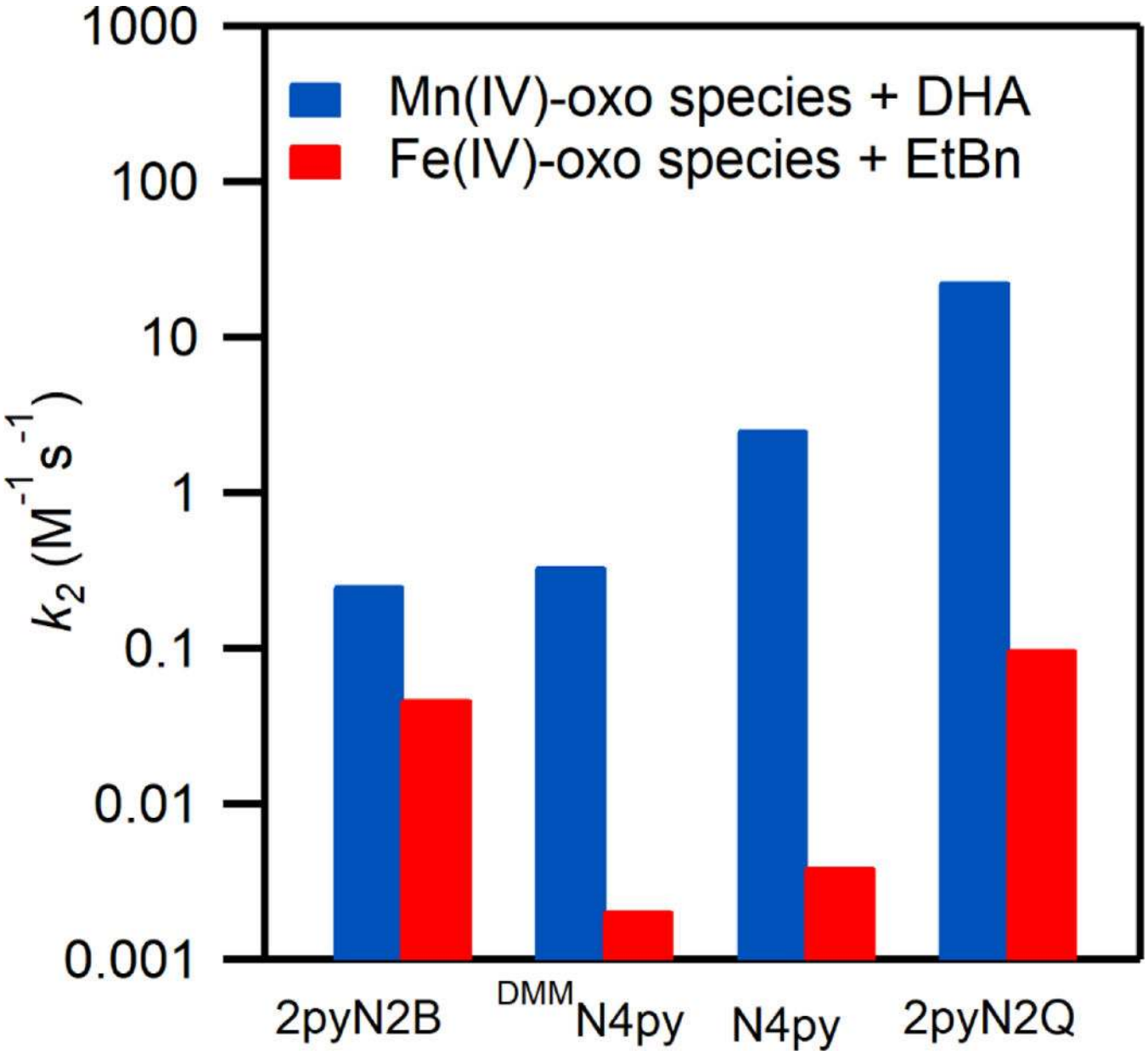

Figure 9.

Blue: Comparison of the rates of reaction of DHA with oxomanganese(IV) species supported by N4py and its derivatives. Red: Comparison of the rates of reaction of ethylbenzene (EtBn) with oxoiron(IV) complexes supported by N4py and its derivatives. The sources of the rate data are as follows: $[Mn^{IV}(O)(^{DMM}N4py)]^{2+}$ and $[Mn^{IV}(O)(2pyN2Q)]^{2+}$ from reference [6]; $[Mn^{IV}(O)(N4py)]^{2+}$ from reference [26]; $[Fe^{IV}(O)(^{DMM}N4py)]^{2+}$ from reference [8]; $[Fe^{IV}(O)(N4py)]^{2+}$ from reference [39]; $[Fe^{IV}(O)(2pyN2B)]^{2+}$from reference [9], $[Fe^{IV}(O)(2pyN2Q)]^{2+}$ from reference.[7] For the oxoiron(IV) complexes, the reactivity trend is slightly different with cumene (Figure S19). Errors for the rates of the Mn^{IV}-oxo complexes are indicated in Table 3. Errors for the Fe^{IV}-oxo rate constants have not all been reported.

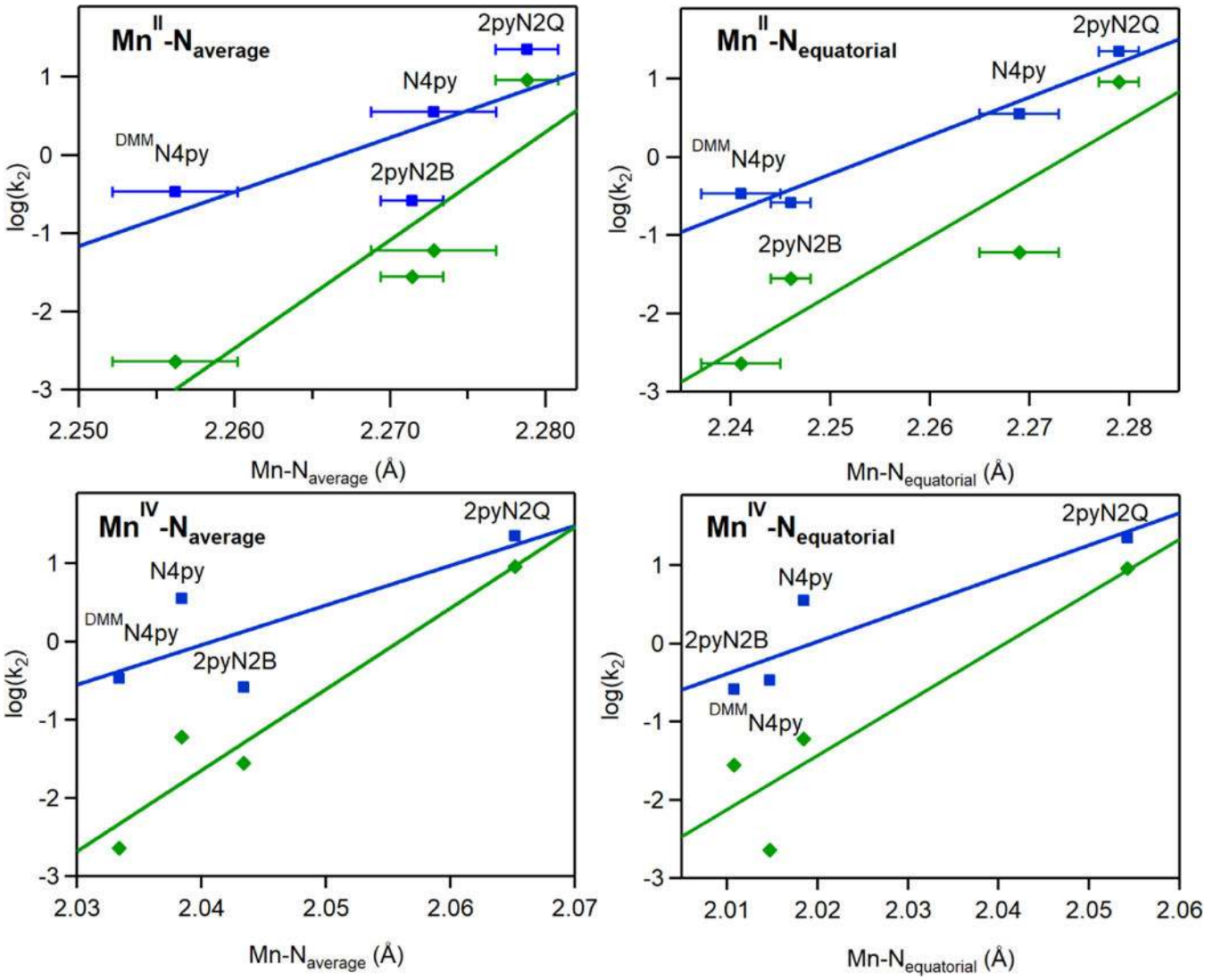

Figure 10.

Comparison of the log(k_2) for DHA (blue) and thioanisole (green) and the average Mn-N distances (left panels) and Mn-N equatorial distances (right panels) for manganese(II) species (top panels) and manganese(IV)-oxo species (bottom panels) supported by N4py and its derivatives. Errors for the reaction rates can be found in Table 3.

Table 1.

Manganese-Ligand Bond Distances (Å) for Mn^{II} Complexes Supported by the 2pyN2B, N4py, ^{DMM}N4py, and 2pyN2Q Ligands.

	$[Mn^{II}(OH_2)(2pyN2B)]^{2+}$	$[Mn^{II}(OTf)(N4py)]^{+}$ [a]	$[Mn^{II}(OTf)(^{DMM}N4py)]^{+}$ [b]	$[Mn^{II}(OH_2)(2pyN2Q)]^{2+}$ [b]
Mn–O	2.087(3)	2.125(3)	2.114(3)	2.091(2)
$Mn–N_X$ [c]	2.193(2)	2.255(4)	2.189(4)	2.250(2)
$Mn–N_X$ [c]	2.193(2)	2.271(4)	2.225(3)	2.265(2)
$Mn–N_{pyridyl}$	2.298(2)	2.271(4)	2.296(4)	2.297(2)
$Mn–N_{pyridyl}$	2.298(2)	2.278(4)	2.293(3)	2.303(2)
$Mn–N_{amine}$	2.375(3)	2.289(4)	2.278(4)	2.279(2)
$Mn–N_{equatorial}$ [d]	2.246	2.269	2.251	2.279
$Mn–N_{total}$ [e]	2.271	2.273	2.256	2.279

[a] From reference 26.

[b] From reference 6.

[c] N_X is $N_{benzimidazolyl}$ for $[Mn^{II}(OH_2)(2pyN2B)]^{2+}$, $N_{pyridyl}$ for $[Mn^{II}(OTf)(N4py)]^{+}$, $N_{3,5\text{-dimethyl-4-methoxypyridyl}}$ for $[Mn^{II}(OTf)(^{DMM}N4py)]^{+}$, and $N_{quinolinyl}$ for $[Mn^{II}(OH_2)(2pyN2Q)]^{2+}$.

[d] Average of the Mn–N bond distances in the equatorial positions.

[e] Average of all Mn–N bond distances.

Table 2.

Electronic Absorption near-IR Band Maxima (nm), Extinction Coefficients (M^{-1} cm^{-1}), $t_{½}$ Values in TFE at 25°C (hours), EPR g-Values, Hyperfine Couplings (mT), XAS Edge and Pre-Edge Energies (eV), XAS Pre-Edge Areas, and CV Peak Potentials (V) for Mn^{IV}-oxo Complexes.

complex	λ_{max}	ε	$t_{½}$	g_{eff} [a]	a [b]	Edge	Pre-edge	area	$E_{p,c}$ [c]
$[Mn^{IV}(O)(^{DMM}N4py)]^{2+}$	920	290	6	4.38	7.7	6550.3	6541.3	19.6	0.61
$[Mn^{IV}(O)(2pyN2B)]^{2+}$	940	250	2.7	5.70	7.0	6549.6	6541.4	14.6	0.47
$[Mn^{IV}(O)(N4py)]^{2+}$	950	230	0.5	4.35	7.6	6550.8	6541.6	18.9	0.80
$[Mn^{IV}(O)(2pyN2Q)]^{2+}$	1180	179	0.2	4.30	7.2	6549.2	6541.2	17.0	1.01

[a] The g_{eff} value of the most intense, positive signal at low field (see Figure S6).

[b] Hyperfine splitting of six-line signals observed near $g = 5.7 – 5.8$ (see Figure S6).

[c] Cathodic peak potential versus SCE. Data for $[Mn^{IV}(O)(N4py)]^{2+}$ comes from reference [26] and data for $[Mn^{IV}(O)(^{DMM}N4py)]^{2+}$ and $[Mn^{IV}(O)(2pyN2Q)]^{2+}$ comes from reference [6].

Table 3.

Second-order Rate Constants (k_2) for the Reactions of Several Mn^{IV}-oxo Complexes with DHA and Thioanisole.

complex[a]	k_2(DHA)[b]	k_2(thioanisole)[b]	Solvent	Temp (°C)	Ref
$[Mn^{IV}(O)(2pyN2Q)]^{2+}$	23(3)	9.2(9)	TFE	25	6
$[Mn^{IV}(O)(N4py)]^{2+}$	3.6(4)	0.060(3)	TFE:CH_3CN (19:1)	25	26
$[Mn^{IV}(O)(^{DMM}N4py)]^{2+}$	0.34(6)	0.0023(4)	TFE:CH_2Cl_2 (DHA); TFE (thioanisole)	25	6
$[Mn^{IV}(O)(2pyN2B)]^{2+}$	0.27(2)	0.028(3)	TFE	25	*c*
$[Mn^{IV}(O)(OH_2)(BQCN)]^{2+}$	0.12	NR[d]	MeCN:H_2O(9:1)	0	36
$[Mn^{IV}(O)(H_3buea)]^{-}$	0.026(2)	NR[d]	DMSO	20	37
$[Mn^{IV}(O)(Bn\text{-}TPEN)]^{2+}$	NR[d]	1.3	TFE:CH_3CN (19:1)	0	38

[a] Ligand abbreviations as follows: BQCN is N,N′-dimethyl-N,N′-bis(8-quinolyl)cyclohexanediamine; H_3buea is tris[(N′-tert-butylureayl)-N-ethyl)]amine; Bn-TPEN is N-benzyl-N,N',N'-tris(2-pyridylmethyl)-1,2-diaminoethane).

[b] $M^{-1}s^{-1}$

[c] This work

[d] Not reported